ANNUAL REVIEWS

Annual Review of Nuclear and Particle Science

Progress in the Glauber Model at Collider Energies

David d'Enterria[1] and Constantin Loizides[2]

[1]EP Department, CERN, 1211 Geneva, Switzerland; email: dde@cern.ch

[2]Physics Division, Oak Ridge National Laboratory, Oak Ridge, Tennessee 37831, USA; email: loizides@cern.ch

Annu. Rev. Nucl. Part. Sci. 2021. 71:315–44

First published as a Review in Advance on June 25, 2021

The *Annual Review of Nuclear and Particle Science* is online at nucl.annualreviews.org

https://doi.org/10.1146/annurev-nucl-102419-060007

Keywords

Glauber model, hadronic collisions, centrality determination, Monte Carlo event generators, inclusive hadronic cross sections

Abstract

We review the theoretical and experimental progress in the Glauber model of multiple nucleon and/or parton scatterings after the last 10–15 years of operation with proton and nuclear beams at the BNL Relativistic Heavy Ion Collider and the CERN Large Hadron Collider. The main developments and the state of the art of the field are summarized. These encompass measurements of the inclusive inelastic proton and nuclear cross sections, advances in the description of the proton and nuclear density profiles and their fluctuations, inclusion of subnucleonic degrees of freedom, experimental procedures and issues related to the determination of the collision centrality, validation of the binary scaling prescription for hard scattering cross sections, and constraints on transport properties of quark–gluon matter from varying initial-state conditions in relativistic hydrodynamics calculations. These advances confirm the validity and usefulness of the Glauber formalism for quantitative studies of quantum chromodynamics matter produced in high-energy collisions of systems, from protons to uranium nuclei, of vastly different size.

Contents

1. INTRODUCTION

The central goal of high-energy nucleus–nucleus (AA) collisions is to study the collective thermodynamic and transport properties of quarks and gluons—the elementary degrees of freedom of the theory of strong interaction, quantum chromodynamics (QCD) (1). Collisions of heavy ions at center-of-mass (CM) energies above tens of GeV provide the only known experimental way to produce a large multibody system of deconfined partons, the quark–gluon plasma (QGP), which is predicted by lattice QCD calculations for energy densities above a critical value of $\varepsilon_c \approx 0.5$ GeV fm^{-3} (2, 3). Such collisions provide the only available known means by which to study in the laboratory the thermodynamics of a system described by a non-Abelian quantum gauge field theory.

Larger transverse spatial overlaps of the two incoming ions lead to a larger volume of the created system, which results in mesoscopic conditions leading to partial (local) thermalization and subsequent collective behavior of the produced partons. Hence, the interpretation of data from high-energy heavy-ion collisions relies on a detailed knowledge of the initial QGP matter distribution that results from the overlap of the two nuclei colliding at a given impact parameter b, complemented by a theoretical modeling of its subsequent space-time evolution. To interpret the experimental observations, it is crucial to derive from the data the transverse size of the created QGP, as well as any event-by-event irregularities that arise from density and/or color fluctuations, because the total and local depositions of energy in the collision chiefly influence the initial conditions and the evolution of the strongly interacting system that is produced.

The generic method to study the properties of QCD matter relies on measuring the distributions of a variety of observables in AA collisions and comparing them with the same measurements in proton–proton (pp) and/or proton–nucleus (pA) collisions, where a QGP is not expected to be produced. Common observables include particle production yields (e.g., light hadrons, heavy quarks, quarkonia, jets, photons) as functions of their transverse momentum (p_T), pseudorapidity (η), and azimuthal angle (ϕ) (4). Carrying out such quantitative comparisons among colliding systems of different sizes requires appropriate normalization of the measured distributions by

using, for instance, the number of participating nucleons ($N_{\rm part}$), the number of independent binary nucleon–nucleon (NN) collisions ($N_{\rm coll}$), the medium transverse area ($A_\perp$), or the system eccentricity (ε_n, given by the nth moments of its azimuthal spatial distribution), as described below.

Computation of the aforementioned quantities typically relies on describing multiple scatterings of the constituents (nucleons, themselves characterized by parton densities) inside the colliding nuclei by using the so-called Glauber formalism, which is named after Roy Glauber's pioneering work on the use of quantum mechanical scattering theory to calculate cross sections in pA and AA collisions (5, 6). The Glauber formalism is based on the geometric (i.e., eikonal) approximation, which assumes that projectile nucleons travel along straight lines (i.e., with negligible momentum exchanges compared with their longitudinal momenta) and undergo multiple independent subcollisions with nucleons in the target. In the original form of the Glauber approach (7–9), the total hadronic cross section of a collision of two nuclei (nucleus A with A nucleons and nucleus B with B nucleons) is given by a $(2A + 2B + 1)$-dimensional integral:

$$\begin{aligned}\sigma_{\rm AB} = &\int \mathrm{d}^2b \int \mathrm{d}^2\mathrm{s}_1^{\rm A}\cdots\mathrm{d}^2\mathrm{s}_A^{\rm A}\mathrm{d}^2\mathrm{s}_1^{\rm B}\cdots\mathrm{d}^2\mathrm{s}_B^{\rm B}\\ &\times T_{\rm A}(\mathbf{s}_1^{\rm A})\cdots T_{\rm A}(\mathbf{s}_A^{\rm A})T_{\rm B}(\mathbf{s}_1^{\rm B})\cdots T_{\rm B}(\mathbf{s}_B^{\rm B})\\ &\times \left\{1-\prod_{j=1}^{B}\prod_{i=1}^{A}\left[1-\sigma(\mathbf{b}-\mathbf{s}_i^{\rm A}+\mathbf{s}_j^{\rm B})\right]\right\},\end{aligned} \quad 1.$$

where $\mathbf{b}$ is the collision impact parameter and $\mathbf{s}$ denotes a position in the transverse plane. The interaction probability $\sigma(\mathbf{s})$ is normalized to give the nucleon–nucleon inelastic cross section $\sigma_{\rm NN} = \int \mathrm{d}^2\mathrm{s}\,\sigma(\mathbf{s})$. The nuclear thickness function $T_{\rm A}(\mathbf{b}) = \int \mathrm{d}z\,\rho_A(\mathbf{b}, z)$ describes the transverse nucleon density by integrating the nuclear density ρ along the longitudinal direction z.

In the so-called optical limit of the Glauber model derived in Reference 9, local density fluctuations and correlations are ignored so that each nucleon in the projectile interacts with the incoming target as a flux tube described with a smooth density. The total cross section then reduces to

$$\sigma_{\rm AB} = \int \mathrm{d}^2b\left\{1-\left[1-\sigma_{\rm NN}T_{\rm AB}(\mathbf{b})\right]^{AB}\right\}, \quad 2.$$

where

$$T_{\rm AB}(\mathbf{b}) = \int \mathrm{d}^2\mathrm{s}\; T_{\rm A}(\mathbf{s})\, T_{\rm B}(\mathbf{s}-\mathbf{b}) \quad 3.$$

is known as the nuclear overlap function, normalized as $\int \mathrm{d}^2b\; T_{\rm AB}(b) = AB$ by integrating over all impact parameters. Equations 1 and 2 give identical results for large enough nuclei and/or for sufficiently small values of $\sigma_{\rm NN}$.

In contrast to optical calculations, Monte Carlo Glauber (MCG) calculations (10–19) evaluate the phase space of Equation 1 stochastically by distributing the A and B nucleons of nuclei A and B, respectively, in coordinate space according to their corresponding nuclear densities and separated by an impact parameter b sampled from $\mathrm{d}\sigma/\mathrm{d}b \propto b$.[1] The nuclear transverse profiles are usually approximated with parameterizations of charge density distributions extracted from low-energy electron–nucleus scattering experiments (20, 21) that, for large spherical nuclei, are usually described by two-parameter Fermi (2pF; also called Woods–Saxon) distributions, $\rho(r) = \rho_0/[1 +$

[1]Hereafter, for simplicity, the impact parameter variable b ($b_{\rm NN}$) is used to denote the transverse distance between the nuclei (or nucleon) centers.

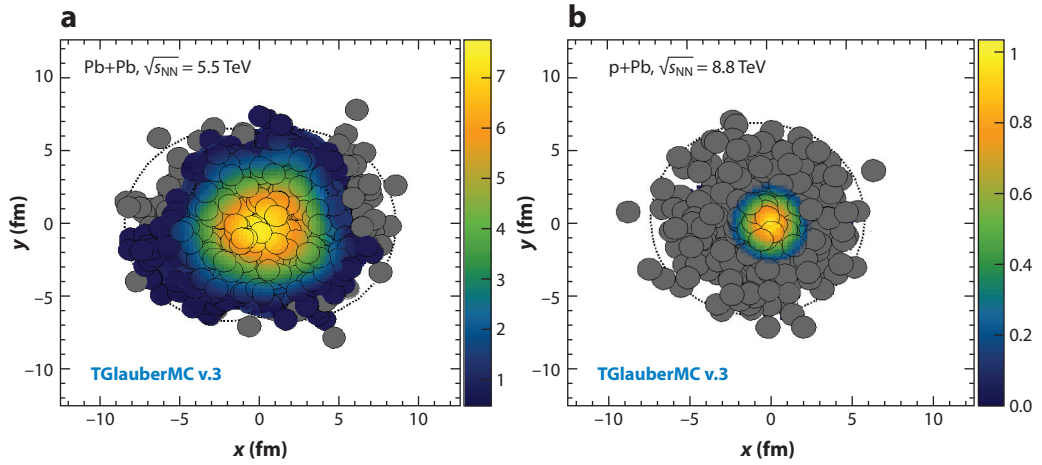

Figure 1

Event displays of initial transverse density profiles in the (x, y) plane of (*a*) Pb+Pb collisions at $\sqrt{s_{NN}} = 5.5$ TeV with a triangular-like shape (5–10% centrality) and (*b*) p+Pb collisions at $\sqrt{s_{NN}} = 8.8$ TeV (0–1% centrality) generated with TGlauberMC (18). The colored bidimensional surfaces indicate the local density (fm^{-2}), following the weighting given by Equation 4 with $\alpha = 0.2$. The gray circles indicate spectator nucleons that do not participate in the collision process.

$\exp(\frac{r-R}{a})$], with half-density radius R and diffusivity a. Following the eikonal approximation, the collision is treated as a sequence of independent binary nucleon–nucleon collisions; that is, the nucleons travel on straight-line trajectories, and their interaction probability does not depend on the number of collisions they have suffered before. In its simplest form, an interaction takes place between two nucleons if the distance d between their centers satisfies $d < \sqrt{\sigma_{NN}/\pi}$. Alternatives to this so-called black disk approximation—using, for example, a Gaussian-like distribution for the nucleon overlap or more complex forms—are also used, as discussed below.

One of the most typical phenomenological applications of the Glauber model is to provide the initial conditions for the number density [or entropy or energy densities, related to the particle density via the QCD equation of state (EoS)] of the medium formed in nuclear collisions as input for hydrodynamics calculations of its subsequent space-time evolution, a crucial element for the observation of near-perfect fluidity of the QGP (22). The initial entropy profile in the transverse plane at midrapidity ($\eta = 0$) is typically assumed to be proportional to a linear combination of the number density of particles produced in soft (with yields assumed to scale as the N_{part} pairs) and hard (scaling as N_{coll}) scatterings (23):

$$s_0(\vec{r}_\perp) \equiv \left.\frac{\mathrm{d}^2 S}{\tau_0\, \mathrm{d}^2 r_\perp \mathrm{d}\eta}\right|_{\eta=0} = \frac{C}{\tau_0}\left[\frac{1-\alpha}{2}\,\rho_{part}(\vec{r}_\perp) + \alpha\,\rho_{coll}(\vec{r}_\perp)\right], \qquad 4.$$

with the relative weight[2] often taken as $\alpha = 0.2$ at the CERN Large Hadron Collider (LHC). Two typical snapshots in the (x, y) plane of the medium formed in Pb+Pb and p+Pb collisions at the LHC are shown in **Figure 1**. Right after the collision, the spectator nucleons (gray circles in **Figure 1**) continue undisturbed with the original longitudinal momenta inside the beam line, whereas the hot and dense QGP formed at midrapidity at the LHC expands longitudinally at about the speed of light and transversely at about 0.6 times the speed of light (24).

[2]The historical wounded nucleon model (WNM) (8) for low-energy heavy-ion collisions assumes an entropy deposit only for each nucleon that engages in one or more inelastic collisions and would correspond to $\alpha = 0$.

Among the quantities derived from Glauber models, the initial azimuthal anisotropy of the QGP system is an important one because it directly propagates to various flow components in the final state through collective hydrodynamic pressure gradients and is thus particularly sensitive to the transport and thermodynamic properties of QCD matter (25). The harmonic eccentricities ε_n of the produced QGP (with $n = 2$ being its ellipticity, $n = 3$ triangularity, etc.) are theoretically defined as

$$\varepsilon_n \equiv \frac{\left|\int r^n e^{in\phi}\, w(r,\phi) r dr d\phi\right|}{\int r^n\, w(r,\phi) r dr d\phi}, \qquad 5.$$

where the weights $w(r, \phi)$ are often taken as the initial density of the medium derived from the Glauber model itself via a linear combination of the underlying $N_{\rm part}$ and $N_{\rm coll}$ distributions, as in Equation 4. Assuming a linear hydrodynamics response, the final harmonic flows determined from the azimuthal distributions of the produced hadrons via $\frac{dN}{d\phi} = \frac{N}{2\pi}\left(1 + \sum_n \{2v_n \cos[n(\phi - \psi_n)]\}\right)$, where ψ_n is the flow plane angle for harmonic flow v_n, are proportional to the initial eccentricity: $v_n = \kappa\varepsilon_n$, with $\kappa \approx 0.2$ depending on the EoS, and deviations being sensitive to the ratio of the medium shear viscosity over entropy density η/s (22, 26–30). Whereas flow studies historically focused on the elliptic component (v_2), analyses of the higher Fourier harmonics have blossomed in recent years because of the large flow signals observed in data from the BNL Relativistic Heavy Ion Collider (RHIC) and the LHC (31–35). A typical Pb+Pb event at the LHC, leading to a medium with a triangular-like profile, is illustrated in **Figure 1*a***.

Another phenomenologically relevant quantity often derived from MCG models is the average path length $L(b)$ in the QGP reference frame, traversed by a given perturbative probe (such as an energetic parton) produced in the collision (36–38). The $L(b)$ dependence of the energy loss suffered by a parton going through a QGP provides valuable information on the jet-quenching mechanism and on the medium properties (39).

All Glauber quantities mentioned above ($T_{\rm AA}$, $N_{\rm coll}$, $N_{\rm part}$, $A_\perp$, ε_n, L) depend on the impact parameter b, which is not directly measurable by the experiments but is monotonically correlated with the overall multiplicity of produced particles in the collision: A smaller impact parameter (i.e., a more central collision) will on average lead to a higher particle multiplicity. The reaction centrality is usually expressed in percentiles of the total inelastic hadronic cross section; 0% indicates "most central" (i.e., fully head-on collisions at $b = 0$ fm), and 100% indicates "most peripheral" (i.e., grazing collisions beyond which there is no QCD interaction[3])—corresponding to $b \gtrsim R_{\rm A} + R_{\rm B}$, where $R_{\rm A}$ and $R_{\rm B}$ are the nuclear radii. Experimental measurements performed in intervals of multiplicity can be mapped to centrality ranges using Glauber-based simulations, and from there they can be extended to all other relevant quantities.

This review aims to summarize the main theoretical and experimental progress achieved in the Glauber formalism in the 15 years since a previous review summarized the status of the field at RHIC energies (41). Key differences at the LHC (with TeV colliding energies per nucleon—up to 50 times larger than those studied at the previous RHIC energy frontier) compared with previous accelerators are driven by the increased importance of the nucleon substructure and by the fact that even the particle multiplicities produced in small collision systems (pp, p+Pb) can reach values as large as those measured in Cu+Cu collisions at 200 GeV (42). An example of the high-density medium formed in p+Pb collisions at the LHC is shown schematically in **Figure 1*b***. Many of the Glauber model developments have occurred in parallel to experimental and theoretical studies of pp, pA, and AA collisions at the LHC as well as prospective studies

[3] Significant electromagnetic interactions of the ions can also happen in ultraperipheral interactions (40) at impact parameters larger than the sum of their nuclear radii.

for future facilities, such as the Future Circular Collider (FCC) (43). This review is organized as follows. Section 2 covers measurements and calculations of the proton and nuclear inelastic cross sections. Section 3 discusses several improvements in the description of the proton and nucleus transverse profiles. Section 4 reviews phenomenological applications of the Glauber model (e.g., for comparisons of hard scattering cross sections among pp, pA, and AA systems) as an underlying framework for heavy-ion Monte Carlo (MC) event generators and to define initial conditions for hydrodynamics evolution models of the collision process. Section 5 examines the experimental methods used to determine the collision centrality and discusses their inherent biases. The review ends with a summary of the main conclusions in Section 6.

2. INELASTIC PROTON AND NUCLEAR CROSS SECTIONS

A key ingredient of all Glauber calculations, via Equations 1 and 2, is the inclusive inelastic nucleon–nucleon cross section, $\sigma_{\rm NN}$, evaluated at the same CM energy $\sqrt{s_{\rm NN}}$ as the pA or AA collision under consideration. The value of $\sigma_{\rm NN}$ receives contributions from (semi)hard parton–parton scatterings (also called minijets), which are computable above a given $p_{\rm T} \approx 2$ GeV cutoff by perturbative QCD (pQCD) approaches, as well as from softer peripheral scatterings of a diffractive nature with a scale not far from $\Lambda_{\rm QCD} \approx 0.2$ GeV. Because of the latter nonperturbative contributions, which cannot be computed from first principles QCD calculations to date, one resorts to phenomenological fits of the experimental data to predict the evolution of $\sigma_{\rm NN}$ as a function of $\sqrt{s_{\rm NN}}$. At high CM energies (above a few tens of GeV), any potential difference due to the valence quark structure is increasingly irrelevant because the bulk of the pQCD cross section proceeds through gluon–gluon scatterings, and all experimental measurements of pp and $\rm p\bar{p}$ (as well as nn and np) collisions can be combined to extract $\sigma_{\rm NN}$.

The collision energy dependence of the inelastic cross section $\sigma_{\rm NN}$ is shown in **Figure 2** from all measurements available to date, including results from fixed-target studies in the range $\sqrt{s_{\rm NN}} \approx$ 10–30 GeV performed in the 1970s–1990s (44); data from $\rm p\bar{p}$ colliders [UA5 at $\sqrt{s} = 200$ and 900 GeV (45); E710 (46, 47) and CDF (48, 49) at $\sqrt{s} = 1.8$ TeV] and pp colliders [STAR at $\sqrt{s} = 200$ GeV (50); ALICE at 7 TeV (51); ATLAS at 7, 8, and 13 TeV (52–55); CMS at 7 and 13 TeV (56, 57); LHCb at 7 and 13 TeV (58, 59); and TOTEM at 2.76, 7, 8, and 13 TeV (60–64)]; and the AUGER result at $\sqrt{s} = 57$ TeV derived from cosmic-ray (proton–air) data (65). The experimental $\sigma_{\rm NN}$ values were obtained either (*a*) via the subtraction $\sigma_{\rm pp} = \sigma_{\rm tot} - \sigma_{\rm el}$, where $\sigma_{\rm tot}$ and $\sigma_{\rm el}$ were accurately measured in dedicated forward Roman pot detectors [TOTEM (60–64) and ALFA (53–55)], or (*b*) from measurements of inelastic particle production data in the central detectors collected with minimum-bias (MB) triggers. The latter measurements are less precise than the former ones because they require an extrapolation, dominated by diffractive contributions, to forward regions of phase space not covered by the detectors. Many MCG codes, such as Glissando (11, 14, 19), use the COMPETE collision energy parameterization of the NN cross section (66), as provided in the PDG 2018 *Review of Particle Physics* (44). However, such a relatively complex multiparameter expression is required only when aiming at a reproduction of the NN cross section data over the full collision energy range that has been experimentally measured (down to $\sqrt{s} \approx 1$ GeV). For the regime of energies relevant at colliders, the $\sqrt{s}$ dependence of the experimental $\sigma_{\rm NN}$ results can be fit to a simpler parameterization, as in Reference 18:

$$\sigma_{\rm NN}(s) = a + b\,\ln^n(s). \qquad 6.$$

This fitting results in $a = 28.84 \pm 0.52$, $b = 0.0458 \pm 0.0167$, and $n = 2.374 \pm 0.123$ with goodness-of-fit over number of degrees of freedom $\chi^2/N_{\rm df} = 0.7$ (and s given in GeV^2 units). **Table 1** shows the derived $\sigma_{\rm NN}$ values relevant for Glauber calculations at RHIC, LHC, and FCC energies.

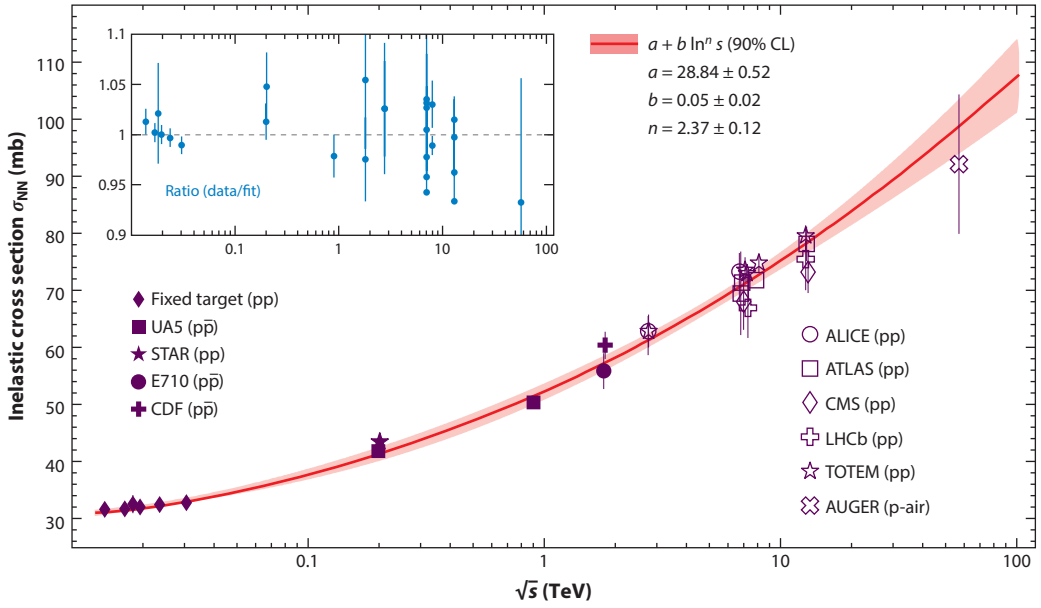

Figure 2

Inelastic pp and p$\bar{p}$ cross sections as a function of center-of-mass energy measured across $\sqrt{s} \approx 10$ GeV–100 TeV fitted to Equation 6. The inset shows the ratio of the data divided by the value of the fit. Data from References 44–65.

The value predicted for the top RHIC energy of $\sqrt{s_{NN}} = 0.2$ TeV, $\sigma_{NN} = 41.3 \pm 1.2$ mb, is consistent with (though more precise than) the value directly measured by STAR ($\sigma_{NN} = 43.82^{+1.39}_{-1.46}$ mb) (50); it is also consistent with the typical 42 ± 3 mb used so far in the RHIC literature (41). At the top FCC energy of $\sqrt{s_{NN}} = 100$ TeV, the expected cross section of $\sigma_{NN} = 107.5 \pm 6.5$ mb is also in agreement with the value derived from the average of various model predictions, 105.1 ± 2.0 mb (67).

From σ_{NN}, one can then use Equation 2 to derive the corresponding values for the pA and AA inelastic cross sections. The σ_{pA} and σ_{AA} results for the p+Pb and Pb+Pb (p+Au and Au+Au for RHIC) systems are listed in the bottom two rows of **Table 1**. The quoted uncertainties account for the propagated σ_{NN} uncertainties plus, in quadrature, the uncertainty resulting from independently varying the density parameters by one standard deviation. The latter uncertainties amount to about 2% and 1.5% for Pb+Pb and p+Pb collisions, respectively, and are dominated by the uncertainty of the neutron skin width. The Glauber calculation gives $\sigma^{MC}_{Pb+Pb} = 7.55 \pm 0.15$ b

Table 1 Inelastic NN, pA, and AA cross sections at collider energies

	$\sqrt{s}$ (TeV)						
Cross section	**0.2**	**5.5**	**8.8**	**14**	**39**	**63**	**100**
σ_{NN} (mb)	41.3 ± 1.2	68.3 ± 1.2	73.6 ± 1.4	79.2 ± 1.9	93.0 ± 3.8	100.2 ± 5.1	107.5 ± 6.5
σ_{pA} (b)	1.75 ± 0.03	2.10 ± 0.03	2.13 ± 0.03	2.17 ± 0.03	2.26 ± 0.04	2.30 ± 0.05	2.35 ± 0.05
σ_{AA} (b)	6.84 ± 0.14	7.64 ± 0.15	7.71 ± 0.16	7.78 ± 0.16	7.93 ± 0.16	8.00 ± 0.17	8.07 ± 0.17

The first row shows values of the nucleon–nucleon inelastic cross section σ_{NN} extracted from Equation 6 and the data plotted in **Figure 2** (44–65). The second and third rows show computed values of the pA and AA hadronic cross sections at center-of-mass energies relevant for collisions at the Relativistic Heavy Ion Collider, the Large Hadron Collider, and the Future Circular Collider. The quoted σ_{pA} and σ_{AA} values are for p+Pb and Pb+Pb collisions everywhere, except for the results at $\sqrt{s_{NN}} = 0.2$ TeV that correspond to p+Au and Au+Au collisions.

at $\sqrt{s_{\rm NN}} = 2.76$ TeV and $\sigma^{\rm MC}_{\rm p+Pb} = 2.09 \pm 0.03$ b at $\sqrt{s_{\rm NN}} = 5.02$ TeV, in good agreement with the measured values of $\sigma_{\rm Pb+Pb} = 7.7 \pm 0.6$ b (68) and $\sigma_{\rm p+Pb} = 2.06 \pm 0.08$ b (69) as well as $\sigma_{\rm p+Pb} = 2.10 \pm 0.07$ b (70). The measured ALICE and CMS inelastic p+Pb and Pb+Pb cross sections thus provide an inclusive validation of the Glauber model at TeV energies. This fact further justifies the common application of the Glauber approach to derive pp cross sections from cosmic-ray proton–air cross section measurements (65).

3. DEVELOPMENTS IN THE DESCRIPTION OF THE INITIAL STATE

In the past 15 years, there have been numerous developments related to the description of the nucleon and nuclei radial profiles in Glauber models, including the incorporation of various sources of event-by-event fluctuations (particularly relevant for collisions involving light ions and/or protons), subnucleonic degrees of freedom, neutron skin effects, and deformed light- and heavy-ion distributions. The most important advances regarding these topics are summarized in this section.

3.1. Proton Transverse Profile

The transverse profile of the proton (or, generically, of the nucleon) is of key importance in many aspects of the Glauber formalism. First, in nuclear collisions, it determines the NN interaction probability, and its realistic description is particularly important for proper description of proton–nucleus results (where intrinsic fluctuations in the proton shape are more relevant than in AA collisions). Second, it is a prime ingredient of MC event generators for pp collisions [e.g., Pythia 8 (71), Herwig++ (72)] to reproduce, through the underlying multiparton interactions (MPIs), the properties of inclusive hadron production both in MB collisions—as a sum of the particle production activity from all, central to peripheral, pp collisions—and in the so-called underlying event (UE) that accompanies hard scatterings at the LHC (73). Third, the proton transverse distribution is also a basic element in calculations of double- and triple-parton scattering cross sections in proton and nuclear collisions, where the effective N-parton scattering (NPS) cross section bears a simple geometric interpretation in terms of powers of the inverse of the integral of the pp overlap function over all impact parameters, $\sigma_{\rm eff,NPS} = [\int {\rm d}^2 b\, T^n_{\rm pp}(\mathbf{b})]^{-1/(n-1)}$ (with $n = 2, 3, \ldots, N$ for double, triple, N scatterings) (74). Efforts to improve the treatment of pp collisions within a Glauber-like approach based on their impact parameter and underlying parton–parton scatterings have attracted increased interest in recent years to interpret high-multiplicity pp results where collective (QGP-like) phenomena have been observed in the data (75–77)—a possibility anticipated in Reference 78.

The most simplistic approach used in Glauber models is to consider a fixed proton shape at all colliding energies; any varying distributions of its parton contents (valence and sea quarks, gluons) and their correlations are disregarded. The simplest form is a hard-sphere parameterization with uniform density, $\rho(r) = \frac{1}{4/3\,\pi R^3}\theta(D - b_{\rm NN})$, where θ is the Heaviside step function, with a radius consistent with electron–proton scattering fits giving a root-mean-square radius $R_{\rm rms} \approx 0.8$ fm (79). A profile more consistent with the proton charge form factor is given by an exponential, $\rho(r) = \frac{1}{8\pi R^3}{\rm e}^{-r/R}$, reproducing to a large extent the spatial distribution of its valence quarks, with $R = R_{\rm rms}/\sqrt{12} = 0.234$ fm. A single Gaussian ansatz, although not very realistic, makes subsequent calculations especially transparent and therefore has been used in some analytical approaches. A double Gaussian ansatz, $\rho(r) \propto \frac{1-\beta}{a_1^3}{\rm e}^{-r^2/a_1^2} + \frac{\beta}{a_2^3}{\rm e}^{-r^2/a_2^2}$, which corresponds to a distribution with a small core region of radius a_2 containing a fraction β of the total matter embedded in a larger region of radius a_1, is a common choice [available, e.g., in the Pythia 8 MC generator (80)].

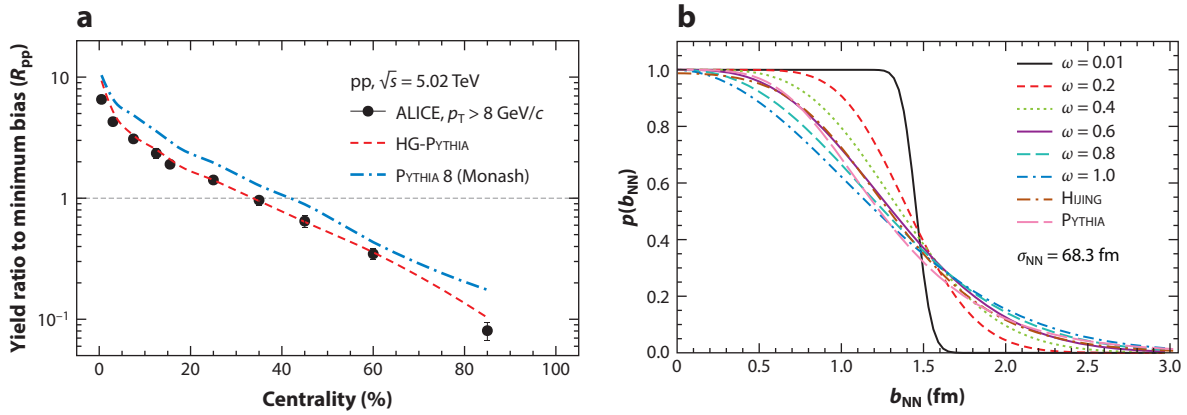

Figure 3

(*a*) Yield of high-p_T charged particles in multiplicity classes measured in pp collisions at $\sqrt{s} = 5.02$ TeV normalized to their minimum-bias yield (82) compared with HG-Pythia and Pythia 8 predictions. (*b*) Nucleon–nucleon collision probability distribution using Equation 9 for various ω values in NN collisions at $\sqrt{s} = 5.02$ TeV compared with the results from the Hijing and Pythia 8 (Monash tune) overlap profiles.

In MC event generators for pp collisions, parameterizations of the impact parameter dependence of the overlap function, rather than the individual radial density of each colliding proton, are usually used. In Pythia 8, the pp overlap is parameterized as

$$T_{pp}(\mathbf{b}) = \frac{m}{2\pi r_p^2 \,\Gamma(2/m)} \exp\left[-(b/r_p)^m\right], \qquad 7.$$

normalized to one, $\int d^2b\, T_{pp}(\mathbf{b}) = 1$, where r_p is a characteristic "radius" of the proton, Γ is the gamma function, and the exponent m varies between a more Gaussian-like ($m \approx 2$) to a more peaked exponential-like ($m \approx 1$) distribution. The popular Pythia 8 Monash parameter settings (tune) use $m = 1.85$ (81). In the Hijing (10) and Herwig++ (72) generators, the pp overlap is approximated by the Fourier transform of the proton electromagnetic form factor as

$$T_{pp}(\mathbf{b}) = \frac{\mu^2}{96\pi} (\mu b)^3 K_3(\mu b), \qquad 8.$$

where $\mu \propto 1/r_p$ is a free parameter, and K_3 is the modified Bessel function of the third kind. In Hijing, $\mu = 3.9/\sqrt{\sigma_{NN}/2\pi}$ is used to describe the dependence of μ on the effective size of the proton.

The importance of properly taking into account the proton transverse profile in pp collisions at LHC energies is illustrated in **Figure 3*a***, which shows the high-p_T hadron yield (normalized to its impact parameter–integrated value) as a function of centrality measured by the ALICE Collaboration at $\sqrt{s} = 5.02$ TeV. The multiplicity classes are obtained by ordering events according to the charged particle response in the ALICE VZERO scintillators ($2.8 < \eta < 5.1$ and $-1.7 < \eta < -3.7$) for events with at least one charged particle produced at midrapidity ($|\eta| < 1$). Central pp collisions feature yields about 10 times larger than those of MB collisions (peripheral pp collision yields are about 10 times smaller), consistent with the expectation from the MPI picture (83). The centrality dependence of the yields is well reproduced by HG-Pythia (84) and (slightly less well) by Pythia 8 (Monash tune), where the former basically corresponds to Pythia with the proton overlap profile given by Equation 8.

The above discussion highlights the importance in MCG simulations of the choice of the NN collision profile, whereby two nucleons collide if their impact parameter is less than a

given distance parameter $D \approx \sqrt{\sigma_{\rm NN}/\pi}$. The simplest collision profiles used are the hard sphere, $p(b_{\rm NN}) = \theta(D - b_{\rm NN})$ (also called black disk), and Gaussian, $p(b) = \exp(-ab^2/D^2)$, with a fitted to reproduce the $\sigma_{\rm NN}$ inelastic cross section (e.g., $a = 0.92$ at RHIC energies) (14), although more involved probabilistic ways to model the NN interaction have been known for a long time (85). At LHC energies, a modification of the collision profile proposed in References 14 and 86 uses a parameterization based on the Euler $\Gamma(z)$ and incomplete $\Gamma(\alpha, z)$ gamma functions:

$$p(b_{\rm NN}) = G\Gamma\left(1/\omega, \frac{Gb_{\rm NN}^2}{D^2\omega}\right) \Big/ \Gamma(1/\omega), \qquad 9.$$

where ω interpolates between the hard sphere ($\omega \to 0$) and Gaussian ($\omega \to 1$) cases. The choice $(G, \omega) = (1, 0.4)$ reproduces the measured $\sigma_{\rm NN} \approx 73$ mb and $\sigma_{\rm pp,\,el} \approx 25$ mb LHC results. **Figure 3*b*** compares NN collision profiles for varying values of the ω parameter and with the PYTHIA 8 Monash and HIJING choices for pp collisions at $\sqrt{s} = 5.02$ TeV. The latter two are obtained via $p(b_{\rm NN}) = 1 - {\rm e}^{-kT_{\rm pp}(b_{\rm NN})}$ so that $2\pi \int p(b_{\rm NN})\, {\rm d}b_{\rm NN}$ gives $\sigma_{\rm NN}$, as is commonly done for profile functions. One can see that the PYTHIA 8 Monash and HIJING profiles correspond approximately to the $\omega = 0.6$ choice in Equation 9.

An extension of the nuclear Glauber approach to pp collisions at the parton level is described in Reference 78, where, by analogy to the nuclear case, the thickness function of a proton with $N_{\rm g}$ partons is written as $T_{\rm p}(x, y) = N_{\rm g} \int {\rm d}z\, \rho(x, y; z)$, normalized to $\int {\rm d}^2b\, T_{\rm p}(b) = N_{\rm g}$. The overlap function of a pp collision at b can be obtained as a convolution over the corresponding thickness functions of each proton normalized to $\int {\rm d}^2b\, T_{\rm pp}(b) = N_{\rm g}^2$. From the partonic cross section $\sigma_{\rm gg}$, one can then define the number of binary parton–parton collisions in a pp collision at impact parameter b: $N_{\rm coll,gg}(b) = \sigma_{\rm gg}\, T_{\rm pp}(b)$. Hence, the probability of an inelastic parton–parton interaction at impact parameter b can be defined as $P_{\rm gg}^{\rm inel}(b) = 1 - {\rm e}^{-\sigma_{\rm gg}\, T_{\rm pp}(b)}$, where the value of $\sigma_{\rm gg}$ is obtained by requiring that the proton–proton inelastic cross section obtained from the pp overlap function, $\int {\rm d}^2b[1 - {\rm e}^{-\sigma_{\rm gg}\, T_{\rm pp}(b)}] = \sigma_{\rm pp}$, match the $\sigma_{\rm pp}^{\rm inel} \approx 40$–$80$ mb values measured at RHIC and LHC energies (**Table 1**). Values of $\sigma_{\rm gg} \approx 6$ mb are used that are consistent with a simplistic perturbative gluon–gluon cross section of $\sigma_{\rm gg} = K \cdot (9/2)\, \pi\, \alpha_s^2/p_{\rm T}^2$ for $\alpha_s \approx 0.5$ at a $p_{\rm T}$ cutoff of order 1 GeV, where $K \approx 2$ is a factor accounting for higher-order pQCD corrections. The final particle multiplicity density in a pp collision follows the same impact parameter dependence as that of the number of binary parton–parton collisions, $N_{\rm coll,\,gg}(b)$, and the average multiplicity in a pp collision integrated over all impact parameters is $\frac{{\rm d}N_{\rm MB}}{{\rm d}\eta} = \frac{{\rm d}N_0}{{\rm d}\eta} \int {\rm d}^2b\, N_{\rm coll,gg}(b)\, P_{\rm gg}^{\rm inel}(b)$; the absolute normalization ${\rm d}N_0/{\rm d}\eta$ is chosen to reproduce the MB particle multiplicity of ${\rm d}N_{\rm MB}/{\rm d}\eta \approx 10$ measured at midrapidity in pp collisions at LHC energies (87).

Other extensions of the nuclear MCG simulations exist that can account for subnucleonic degrees of freedom (e.g., three constituent valence quarks) (16, 17, 19, 88, 89). The number of partonic constituents and the way to distribute them in pA and AA collisions—between the two extremes of being bound to individual nucleons (according, e.g., to a radially exponential nucleon form factor) or freely distributed over the nucleus (following a global 2pF profile)—must be chosen so as to reproduce basic experimental quantities (inelastic cross sections $\sigma_{\rm NN}$, $\sigma_{\rm pA}$, $\sigma_{\rm AA}$, overall particle multiplicities) and have a different impact on the event ellipticity and triangularity. Accounting for subnucleonic degrees of freedom is particularly important for generating realistic initial conditions for small QGP systems at the LHC, as discussed in Section 4.3.

3.2. Fluctuations and Correlations

Traditionally, Glauber studies dealt only with average nucleon and nuclear transverse densities, but in the last decade more studies have incorporated event-by-event shape fluctuations generated by various underlying mechanisms. Such developments have been largely motivated by an

increasing number of experimental observations that pointed to the need for enhanced eccentricity fluctuations in order to explain, for instance, the large azimuthal harmonics—direct (90), elliptic (91), and triangular (29, 31–35) flows—observed in the data.

There are two obvious sources of fluctuations in MCG simulations: fluctuations in the positions of nucleons within the nucleus and fluctuations at the subnucleonic level. The former are, in principle, properly accounted for by conventional MCG simulations (92), and we thus focus mostly on the latter. Nucleons are composite quantum mechanical systems with varying spatial and momentum configurations of their internal quark and gluon constituents, and the overall transverse area occupied by their color fields changes event-by-event—a phenomenon often referred to as color fluctuations (CFs) (93–95). Such fluctuations can lead to potentially large changes in the effective collision-by-collision nucleon transverse size that are often not accounted for in MCG codes, notably when the NN interaction is approximated by a simple black disk approach (see above). Whereas such CFs tend to average out in central AA collisions, they are of importance for pp and pA collisions. CFs have been evaluated theoretically in terms of the cross section for inelastic diffractive processes in pN scattering—a method often referred to as the Glauber–Gribov approach (96), generalized to the nuclear case (93)—and have been phenomenologically encoded into an event-by-event variation of σ_{NN} given by a probability distribution of the following form:

$$P_{\sigma}(\sigma_{\mathrm{NN}}) = C\frac{\sigma_{\mathrm{NN}}}{\sigma_{\mathrm{NN}}+\sigma_0}\exp^{-\left(\frac{\sigma_{\mathrm{NN}}-\sigma_0}{\sigma_0\,\Omega}\right)^2}, \qquad 10.$$

where σ_0 denotes the mean σ_{NN} value, and Ω denotes its (normalized) width. The normalization C is computed from the provided input (mean σ_{NN} and Ω) requiring $\int \sigma P \mathrm{d}\sigma / \int P \mathrm{d}\sigma = \sigma_0$, with the dispersion given by the ratio of inelastic diffraction over the elastic cross section at $t = 0$ (zero momentum exchange). Variations of the nucleon interaction strength naturally lead to increased fluctuations in the number of participant nucleons and binary nucleon collisions (e.g., longer tails in the N_{part} and N_{coll} distributions) compared with the pure eikonal picture. Example distributions for p+Pb collisions at the LHC with varying width values $\Omega = 0$, 0.5, and 1.0 are shown in **Figure 4*a***. Microscopic refinements in the MCG treatment of fluctuations from diffractive scatterings in pA collisions have been discussed in Reference 97, which proposed a log-normal parameterization instead of Equation 10. In addition, CFs explain the existence of partonic configurations of the nucleon with smaller-than-average interaction strength that lead to observable differences in the centrality dependence of single-jet production in d+Au and p+Pb collisions observed in data from RHIC and the LHC (98, 99). Such events are characterized by a configuration in which a large fraction of the proton momentum is carried by a single parton (e.g., $x \gtrsim 0.1$) that is more spatially compact than the average, and their interaction strength is thereby reduced with respect to the eikonal limit (100). The standard MCG models underestimate the associated number of peripheral events with low hadronic activity, while they overestimate the central ones with large hadronic activity, although inclusive jet production rates remain unmodified.

Most Glauber-like calculations are based on the pure eikonal approximation and disregard higher-order terms of the expansion given by Equation 1 that account for short-range two- and three-nucleon correlations (many-nucleon correlations are further suppressed). The impact of realistically correlated NN configurations (centrally correlated nucleon configurations, two-body full correlations, three-body chains) on the medium eccentricity has been studied in Reference 85, which found that their combined effects cancel out and bring the results close to the case of no correlations. The impact of NN correlations and their interplay with diffractive effects on N_{coll} have been estimated in Reference 101. The authors found that such correlations decrease by a few percent the N_{coll} values (and increase by a few percent the σ_{pA} and σ_{AA} results) compared with the

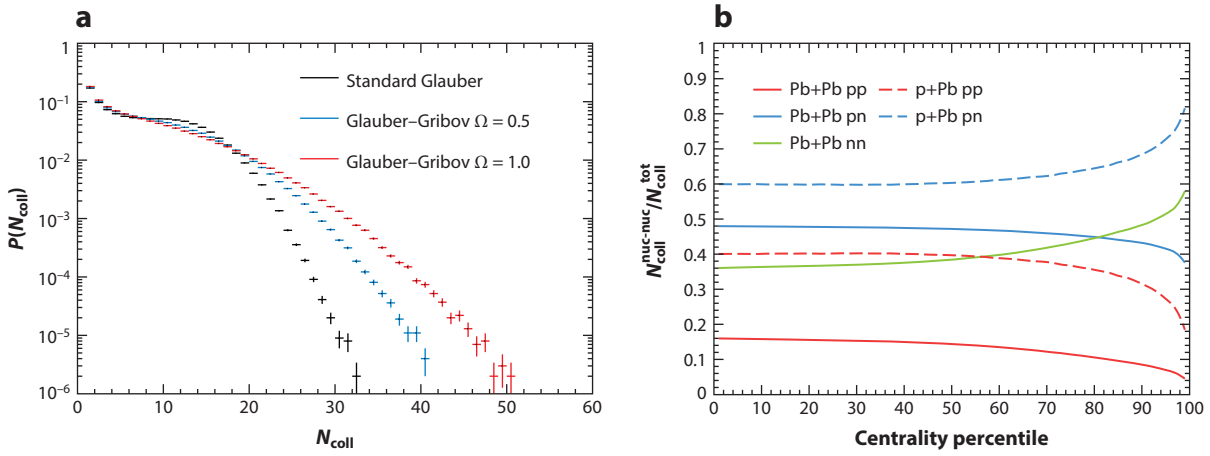

Figure 4

(*a*) Comparison of the N_{coll} distributions for p+Pb collisions at the CERN Large Hadron Collider with different values of the Glauber–Gribov corrections given by $\Omega = 0$, 0.5, and 1.0 in Equation 10. (*b*) Average fraction of pp, pn, and nn collisions for Pb+Pb (*solid curves*) and p+Pb (*dashed curves*) obtained by incorporating a neutron skin in the Pb density profile. Both distributions were obtained with TGlauberMC. Panel *b* adapted from Reference 18 (CC BY 4.0, copyright American Physical Society).

pure Glauber results but that such effects are canceled out when taking into account diffractive (i.e., Gribov inelastic shadowing) corrections that act in the opposite direction. The number of nucleons that are diffractively excited in the multiple collisions but revert back to their ground state before the scattering process is completed both increases the nuclear transparency (i.e., reduces the nuclear cross section) and reduces the N_{coll} results back to the values obtained with the conventional Glauber codes. Another possible source of correlations in MCG simulations is due to the recentering procedure (18) by which the MC setup of the initial nuclear profile without nucleon overlaps is done in such a way that the CM of each nucleus is fixed at a given location in each event. Those correlations are found to be small, in particular for large nuclei (92). Correlations at the parton level due to the interference of same-color gluons from different nucleons, evaluated with the DIPSY generator (102) based on a BFKL resummation of small-x dipoles (103), were found to have only a small effect (i.e., a few percent) for pA collisions with heavy nuclei.

3.3. Neutron Skin and Isospin Effects

The transverse profile of nucleons inside a nucleus is commonly described by a single 2pF distribution. This ansatz, based on studies of the charge distribution (protons) of nuclei with electromagnetic probes, is however not supported by measurements with strongly interacting probes. The latter prefer instead two nonidentical distributions for protons and neutrons (104), in particular at the surface of heavy stable neutron-rich nuclei, such as ^{208}Pb with a neutron excess of $N/Z \approx 1.5$ (105, 106). These differences appear because protons around the center of the nucleus feel their common electromagnetic repulsion from all directions, which results in an electrostatic equilibrium at a constant charge density, but the outermost protons at $r \gtrsim 6$ fm, where the nucleon density begins to drop, need additional skin or halo neutrons in the periphery to counteract the outward Coulomb repulsion and maintain a sufficient nuclear surface tension.

The nominal heavy-ion species at the LHC is ^{208}Pb, the heaviest stable doubly magic nucleus and one of the most intensively studied isotopes. While the average charge radius of ^{208}Pb is known to within ±0.02 fm (21, 107), past estimates placed the uncertainty in the neutron radius at about

± 0.2 fm (108). Neutron point density parameters of $R_n = 6.67 \pm 0.03$ (stat.) fm and $a_n = 0.55 \pm 0.01$ (stat.) $^{+0.02}_{-0.03}$ (syst.) fm have been measured by the Crystal Ball Collaboration via coherent pion photoproduction (106), while the CERN LEAR experiment reports comparable values of $R_n = 6.684 \pm 0.020$ (stat.) fm and $a_n = 0.571$ fm derived from antiproton–nucleus interactions coupled with radiochemistry techniques (105). These data favor a peripheral neutron distribution in the form of a neutron halo rather than a neutron skin; that is, the neutron distribution is slightly broader than the proton one because of its larger diffusivity ($a_n - a_p \approx 0.1$ fm), but it has the same half-radius as the proton distribution ($R_p \approx R_n \approx 6.7$ fm). The combined point density distribution for protons and neutrons has been implemented in recent MCG simulations (18) via the weighted sum of the individual 2pF distributions. For peripheral Pb+Pb collisions, this results in a maximum ~4% increase in N_{coll} and approximately half this percentage for p+Pb collisions, largely driven by the increase of the central radius in the double 2pF (D2pF) compared with the 2pF parameterization. If one focuses instead on the transverse distribution of the underlying d quarks, the dominant flavor in neutrons, larger effects are expected for precise phenomenological studies of isospin-dependent gauge boson (γ, $W^{\pm}$, and Z) cross sections in nuclear compared with proton collisions (109–112). **Figure 4*b*** shows the average fraction of pp, pn, and nn scatterings for Pb+Pb and p+Pb collisions versus centrality, illustrating the increasing relevance of the neutron density for peripheral collisions.

3.4. Light and Heavy Deformed Nuclei

For a number of years, the RHIC machine has provided collisions with a variety of ions beyond the nominal gold nucleus—ranging from the lightest species, such as deuteron (^{2}H) and helium-3 (^{3}He) (113), to the heaviest ones, such as uranium (U) (114)—as a means to study the system size dependence of various QGP-related signals. As mentioned above, for spherical nuclei, the probability density distribution in MCG models is sampled from the underlying 2pF or D2pF radial probability functions and is taken to be uniform in azimuthal and polar angles, but light species such as ^{2}H, ^{3}He, tritium (^{3}H), helium-4 (^{4}He), carbon (^{12}C), oxygen (^{16}O), and sulfur (^{32}S) have dedicated parameterizations of their transverse profiles. For deuteron, the Hulthén form $\rho(r') = \rho_0(\frac{e^{-ar'} - e^{-br'}}{r'})^2$, with $a = 0.228$ fm^{-1} and $b = 1.177$ fm^{-1}, and $r' = 2r$ denoting the distance between the proton and neutron, is often employed (115–117). For ^{3}H and ^{3}He nuclei, configurations are computed from Green's function MC calculations using the AV18/UIX Hamiltonian, which correctly sample the position of the three nucleons, including their correlations (118). Similarly, results of wavefunction-based calculations are available for ^{4}He, ^{12}C, and ^{16}O (119). For slightly deformed nuclei, such as sulfur, the Fermi distribution is modified with an extra parameter w and a Gaussian term, $\rho(r) = \rho_0 \frac{1+w(r/R)^2}{1+\exp(\frac{r^2-R^2}{a^2})}$. Details for all relevant parameterizations can be found in References 15, 119, and 120.

Description of the transverse profile of heavy deformed nuclei starts with the 2pF expressions modified with an expansion of R in spherical harmonics, $\rho(r) = \rho_0(1 + \exp\frac{[r - R(1+\beta_2 Y_{20} + \beta_4 Y_{40})]}{a})^{-1}$, with $Y_{20} = \sqrt{\frac{5}{16\pi}}[3\cos^2(\theta) - 1]$, $Y_{40} = \frac{3}{16\sqrt{\pi}}[35\cos^4(\theta) - 30\cos^2(\theta) + 3]$, and deformation parameters β_2 (quadrupole) and β_4 (hexadecapole) (21). The higher harmonic eccentricities ε_n of the initial QGP produced in collisions of deformed nuclei, such as U, are particularly sensitive to the parameterization of their profiles. A proper description of collisions of heavy deformed nuclei also must account for their relative, tip-on-tip and side-on-side, orientations. Tip-on-tip collisions produce a smaller elliptic flow but larger particle multiplicities (entropy densities), whereas side-on-side collisions generate a larger elliptic flow but a smaller multiplicity. The scaling of $v_{2,3}$ flows with multiplicity in ultracentral collisions (0–1% centrality percentile) in small

and deformed systems produced in U+U, d+Au, ^{9}Be+Au, ^{9}Be+^{9}Be, ^{3}He+^{3}He, and ^{3}He+Au collisions at RHIC energies, including and excluding fluctuations from subnucleonic degrees of freedom, has been theoretically studied in References 121 and 122. This work indicates that such collisions can help discriminate between different initial entropy densities of the QGP medium formed at RHIC and the LHC (123, 124). Implications for the extraction of QGP transport properties, such as its viscosity, are further developed in Section 4.3.

4. PHENOMENOLOGICAL APPLICATIONS

The Glauber model has multiple important phenomenological applications in nuclear collisions at colliders. We consider three typical cases here: (*a*) in the definition of the baseline scalings for comparing hard scattering cross sections in pp, pA, and AA collisions; (*b*) as an underlying framework for MC event generators used in high-energy heavy-ion and cosmic-ray physics; and (*c*) to provide realistic initial-state conditions of the created QGP for subsequent space-time evolution in hydrodynamics codes. Below, we succinctly review the basic ideas and latest progress in these three areas.

4.1. Binary Scaling for Hard Scatterings

One of the most common uses of the Glauber model is to properly normalize the fractional cross sections or yields for the production of a given particle in hard scattering processes (i.e., partonic processes characterized by mass and/or p_T scales above a few GeV) in AA and pA collisions so that they can be compared with those expected in the simpler pp collisions where no QGP formation is, in principle, expected. For pQCD observables that do not suffer any final-state effects, the assumption of binary scaling allows the extraction of modifications of the nuclear parton distribution functions (PDFs) compared with the free proton ones.

It is informative to recall the basic scaling rules for perturbative scatterings in nuclear collisions (125, 126). For a given hard process A+B $\rightarrow h + X$, from the generic Equation 2 for the inclusive AA cross section, one obtains the following relationship between pp and nuclear collisions:

$$\sigma_{AB}^{hard} = \int d^2b\, \sigma_{NN}^{hard}\, T_{AB}(b), \text{ and, therefore, } \sigma_{AB,MB}^{hard} = A \cdot B \cdot \sigma_{NN}^{hard}, \qquad 11.$$

where the second expression for the inclusive hard cross section is obtained by integrating the first expression over the impact parameter. The associated MB invariant yield per nuclear collision, $N_{AB}^{hard} = \sigma_{AB}^{hard}/\sigma_{AB}$, for a given hard process in an AB collision compared with that of a pp collision, is $\langle N_{AB}^{hard}\rangle_{MB} = \frac{A\cdot B}{\sigma_{AB}} \cdot \sigma_{NN}^{hard}$, where σ_{AB} is the inclusive inelastic AB cross section given by Equation 2. The average nuclear overlap function for MB collisions is

$$\langle T_{AB}\rangle_{MB} \equiv \frac{\int d^2b\, T_{AB}(b)}{\int d^2b} = \frac{A \cdot B}{\sigma_{AB}}. \qquad 12.$$

The corresponding expressions for any given impact parameter b can be obtained by multiplying each nucleon in nucleus A with the density along the z direction in nucleus B, integrated over nucleons in nucleus A:

$$N_{AB}^{hard}(b) = \sigma_{NN}^{hard} \int d^2\mathbf{s} \int \rho_A(\mathbf{s}, z') \int dz''dz'\, \rho_B(|\mathbf{b}-\mathbf{s}|, z'') \equiv \sigma_{NN}^{hard} \cdot T_{AB}(b). \qquad 13.$$

Similarly, one obtains a useful expression for the probability of an inelastic NN collision or, equivalently, for the number of binary inelastic collisions, N_{coll}, in a nucleus–nucleus collision at impact parameter b:

$$N_{coll}(b) = \sigma_{NN} \cdot T_{AB}(b). \qquad 14.$$

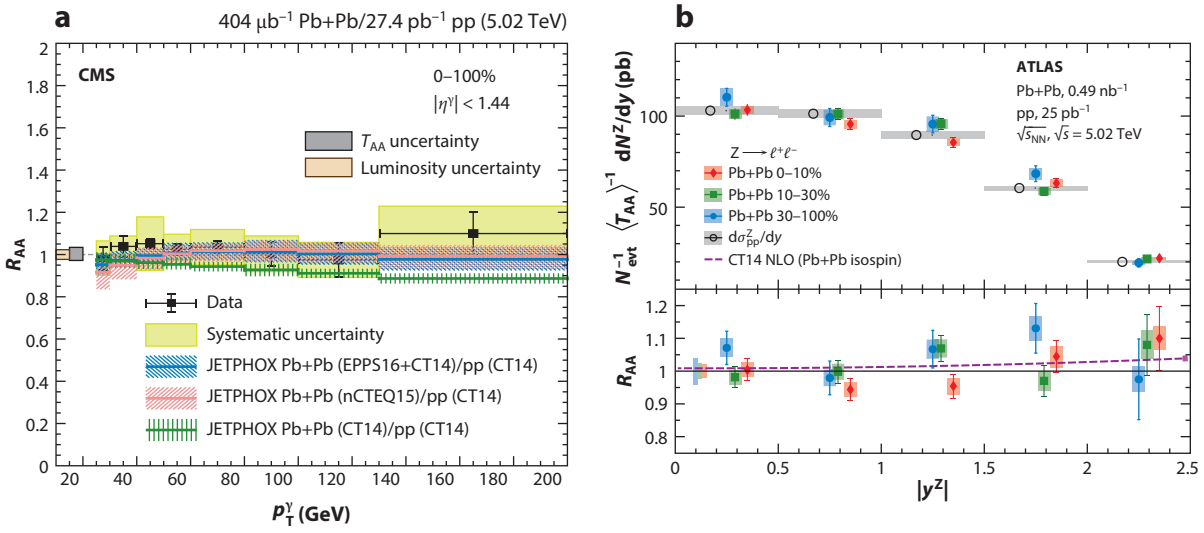

Figure 5

Nuclear modification factors R_{AA} measured for (*a*) isolated photons as a function of p_T^γ (130) and (*b*) Z bosons as a function of rapidity (136) in Pb+Pb collisions at the CERN Large Hadron Collider compared with perturbative quantum chromodynamics NLO calculations with nuclear parton distribution functions. Abbreviation: NLO, next-to-leading order. Panel *a* adapted from Reference 130 (CC BY 4.0, copyright CERN). Panel *b* adapted from Reference 136 (CC BY 4.0, copyright CERN).

From this last expression, one can see that the nuclear overlap function, $T_{AB}(b) = N_{coll}(b)/\sigma_{NN}$ [mb^{-1}], can be thought of as the hard scattering integrated luminosity (i.e., the number of hard collisions per unit of cross section) per AB collision at a given impact parameter.

The expressions above allow one to write the standard binary (or point-like) collision scaling formula that relates the hard scattering yields in nuclear and proton collisions as $N_{AB}(b) = N_{coll}(b) \cdot N_{pp}$. The nuclear modification factor for hard scattering processes is thereby defined as the ratio of AA over scaled pp cross sections and/or yields (here, differential in p_T and η) as

$$R_{AB}(p_T, \eta) = \frac{d^2\sigma_{AB}/dp_T d\eta}{(A \cdot B)\, d^2\sigma_{pp}/dp_T d\eta} \qquad 15.$$

for MB collisions, and it is dependent on b as

$$R_{AB}(p_T, \eta; b) = \frac{d^2N_{AB}(b)/dp_T d\eta}{T_{AB}(b)\, d^2\sigma_{pp}/dp_T d\eta} = \frac{d^2N_{AB}(b)/dp_T d\eta}{N_{coll}(b)\, dN_{pp}/dp_T d\eta}. \qquad 16.$$

In the absence of any final- and/or initial-state effects, one expects $R_{AB} = 1$ for any hard scattering process. The equality of Equations 15 or 16 to unity, modulo few-percent nuclear PDF effects (see below), for colorless hard probes that do not suffer final-state interactions in the produced QGP, was confirmed previously in heavy-ion collisions at SPS and RHIC as well as (more recently) at LHC energies. This, in itself, constitutes a validation of the basic assumptions of the Glauber model itself. Prominent examples include the production yields of photons (127–130) and W and Z bosons (131–138) in p+Pb and Pb+Pb collisions.

Figure 5 shows the R_{AA} values measured for isolated photons (130) and Z bosons (136) as functions of p_T^γ and rapidity $|y^Z|$, respectively, in Pb+Pb collisions at the LHC. Both ratios are around unity with small variations due to nuclear PDF modifications related either to the increased number of d quarks in the Pb nucleus compared with protons (isospin effects) and/or to few-percent (anti)shadowing effects at the large virtualities ($Q \approx p_T^\gamma, m_Z$) probed in the underlying

partonic scatterings. Under the key assumption of binary scaling, the precision of the Pb+Pb data (experimental uncertainties of a few percent in the case of electroweak gauge bosons) allows the derivation of the EPPS16 (139), nCTEQ15 (140), and nNNPDF2.0 (141) nuclear PDFs at next-to-leading order (NLO) and, more recently, also at next-to-next-to-leading order (NNLO) (142) accuracy, through global fits combining nuclear deep inelastic scattering (DIS) and LHC electroweak boson data. Precision electroweak boson measurements in Pb+Pb collisions can also be used to derive a data-driven normalization, in principle independent of the Glauber model, for any other measurements of hard probes in Pb+Pb collisions, as explored in Reference 143.

4.2. Heavy-Ion Monte Carlo Event Generators

All existing generic event generators of ultrarelativistic pA and AA collisions—such as Hijing 1.0 (10), Hijing 2.0 (144), Epos-LHC (145), Ampt (146), Qgsjet-II (147), Dpmjet-III (148), and the more recent Pythia 8–based (149) Angantyr (150) code—internally rely on a Glauber picture to model the early stage of the collision through the proper computation of the number of inelastic subcollisions for any reaction centrality. The main differences among models arise from their treatment of the underlying (semi)hard scatterings: minijets in the case of the Hijing, Angantyr, and Ampt codes, which are mostly used in collider physics; and Regge–Gribov cut pomerons (also called parton ladders, giving rise to one or two strings spanned between two colliding nucleons, or between a nucleon and another pomeron) in the case of the Epos-LHC, Qgsjet-II, and Dpmjet-III codes, which are mostly used in cosmic-ray physics (151). The final hadronization of partons or strings is carried out via (variations of) the Lund fragmentation model (152) in all generators.

The Hijing generator relies on the eikonal approach to determine the number of inelastic subcollisions of two types: soft NN collisions treated as in the Fritiof approach (153), and (multiple) hard parton–parton collisions treated perturbatively as in Pythia. The transverse momentum cutoff $p_{\mathrm{T},0} \approx 2$ GeV that separates hard from soft scatterings increases slowly with collision energy (logarithmically, similar to the evolution of the inelastic cross section given by Equation 6) so that the total number of minijets per unit transverse area satisfies $p_{\mathrm{T},0}^2/\pi > T_{\mathrm{AA}}(b)\,\sigma_{\mathrm{hard}}/(\pi R_{\mathrm{A}}^2)$, where σ_{hard} is the pQCD cross section for $2 \to 2$ parton scatterings, and $T_{\mathrm{AA}}(b)$ is the overlap function of the AA collision. The probability for an inelastic NN collision is given by $\mathrm{d}\sigma_{\mathrm{NN}} = 2\pi\, b_{\mathrm{NN}}\, \mathrm{d}b_{\mathrm{NN}}\, [1 - \mathrm{e}^{-(\sigma_{\mathrm{soft}}+\sigma_{\mathrm{hard}})\, T_{\mathrm{NN}}(b_{\mathrm{NN}})}]$ with $T_{\mathrm{NN}}(b_{\mathrm{NN}})$ given by Equation 8. At $\sqrt{s_{\mathrm{NN}}} = 0.2$ and 5.02 TeV, $\sigma_{\mathrm{hard}} = 11.7$ and 124.3 mb, respectively, and the associated number of MPIs per NN interaction is distributed as $P(N_{\mathrm{NN}}^{\mathrm{hard}}) \propto \mathrm{e}^{-\langle N_{\mathrm{NN}}^{\mathrm{hard}} \rangle}$, around the average number of hard scatterings determined by b_{NN} and given by $\langle N_{\mathrm{NN}}^{\mathrm{hard}} \rangle = \sigma_{\mathrm{hard}}\, T_{\mathrm{NN}}(b_{\mathrm{NN}})$. The average number of hard collisions per NN collision increases from $\langle N_{\mathrm{NN}}^{\mathrm{hard}} \rangle = 0.28$ to 1.77 between $\sqrt{s_{\mathrm{NN}}} = 0.2$ and 5.02 TeV. The total number of hard scatterings for an AA collision is then obtained by summing over all NN collisions in the MCG; that is, $N_{\mathrm{hard}} = \sum_{i=1}^{N_{\mathrm{coll}}} \left(N_{\mathrm{NN}}^{\mathrm{hard}}\right)_i$.

The Ampt code directly uses the Glauber initial conditions generated by Hijing as input for its parton cascade evolution. The most recent heavy-ion event generator is Angantyr, which follows a Glauber approach similar to that of Hijing but further accounts for Glauber–Gribov corrections by dividing up each inelastic subcollision as either single diffractive, double diffractive, or absorptive (i.e., nondiffractive). CF effects are implemented through a model with fluctuating nucleon radii, resulting in a fluctuating NN cross section inspired by the approach of Reference 94.

At variance with other generators, Epos-LHC keeps track of how many times a given nucleon interacts with nucleons from the other nucleus and separates them event-by-event into the "core" (nucleons that collided more than once) and "corona" (nucleons that interacted exactly once). Event-by-event, a fraction of the string segments that do not overlap (i.e., corona) fragment into hadrons normally, following the Lund string model, whereas the other clusters with high density of

strings are used to create a (QGP-like) core that can flow and hadronize collectively. Such a two-component core–corona medium leads to a consistent reproduction of the particle multiplicity dependence of a number of observables (e.g., $<p_T>$, ratio of different hadron yields) in pp, pA, and AA collisions (145). The subsequent collective expansion of the medium, which is defined by the initial core particle density, is taken care of by relativistic hydrodynamics equations.

Apart from the hadronic MC event generators mentioned above, generators of ultraperipheral (photon-induced) nuclear collisions, such as STARLIGHT (154) and SUPERCHIC 3 (155), also employ a Glauber approach to determine the nonhadronic overlap probability needed to compute the cross sections of purely exclusive final states. In STARLIGHT, the probability of having no hadronic interactions is given by $P_{\mathrm{no.had}}(b) = \mathrm{e}^{-\sigma_{\mathrm{NN}} T_{\mathrm{A}}(b)}$, where $T_{\mathrm{A}}(b)$ is the nuclear thickness function. For large nuclei, applying this probability function is roughly equivalent to imposing a $b > R_{\mathrm{A}}$ condition on their photon flux. This probability is also used when the photon is emitted by the proton, leading to an effective γ flux in pA collisions that is considerably smaller than one calculated directly from the electromagnetic proton form factor.

4.3. Initial Conditions for Quark–Gluon Plasma Hydrodynamics Evolution Calculations

The strongly interacting medium created in AA collisions at the LHC is a dynamical system that expands, cools down, and transforms into a hadron gas at times around $\tau = 10$–15 fm/c (27). Under such conditions, the QGP properties can be extracted only by comparing the experimental measurements of the hadronic final state with theoretical predictions that include a model of the full space-time evolution of the heavy-ion collision process (156). The current state of the art for the QGP evolution is given by three-dimensional viscous relativistic fluid dynamics calculations (26, 29, 30, 157, 158)—where the plasma thermodynamic properties evolve according to the lattice QCD EoS (2, 3) with nonideal corrections encoded in the medium shear viscosity η—matched to a hadron transport cascade [often, the UrQMD code (159)] once the energy density drops below ε_c. The largest source of uncertainty in the extraction of medium properties from data–theory comparisons lies in the description of the initial state of the QGP (28), which we discuss below.

Hydrodynamics models start their evolution at τ_0 from a given input entropy (or energy) density in the transverse plane $s_0(\vec{r}_\perp)$. In principle, such initial conditions should be consistently derived by solving the nonequilibrium evolution of the matter created in the first parton–parton interactions, but achieving thermalization of the interacting fields in ultrashort $\mathcal{O}(1\ \mathrm{fm})$ timescales remains a difficult theoretical problem in heavy-ion physics (160). Therefore, one assumes that the produced matter has (pre)equilibrated, and the initial conditions are usually given by one of the following:

1. the number density of produced gluons after the primary collisions, via $s_0(\vec{r}_\perp) \propto \mathrm{d}^2 N_{\mathrm{g}}/(\tau_0 \mathrm{d}^2 r_\perp \mathrm{d}\eta)$, derived analytically—for instance, in models such as MC-KLN (161, 162) and IP-Glasma (163, 164) based on the color glass condensate (CGC) effective theory for parton saturation in heavy-ion collisions (165)—or by pQCD NLO calculations with ad hoc parton saturation, such as EKRT (166, 167); or
2. MCG profiles, such as those shown in **Figure 1**, obtained with the ansatz given by Equation 4 with α adjusted to match the observed multiplicity distributions, or similarly generated with one of the MC event simulations (e.g., HIJING, EPOS) discussed in Section 4.2.

The corresponding local deposition of the entropy density from the underlying (parton or nucleon) collisions, and thereby the transverse area and azimuthal anisotropies of the produced medium, is then model dependent. The T$_{\mathrm{R}}$ENTo approach (168) has parameterized all different

approaches with a generic function of the participant target and projectile thickness functions $T_{A,B}^{part}$ as

$$s \propto \left(\frac{T_A^{part} + T_B^{part}}{2} \right)^{1/p} \qquad 17.$$

with a continuous parameter p that effectively interpolates among different entropy deposition schemes. For $p = (1, 0, -1)$, this generalized mean reduces to arithmetic $(T_A^{part} + T_B^{part})/2$, geometric $\sqrt{T_A^{part} T_B^{part}}$, and harmonic $[2\, T_A^{part} T_B^{part}/(T_A^{part} + T_B^{part})]$ means, while for $p \to \pm\infty$ it asymptotes to maximum $s \propto \max(T_A^{part}, T_B^{part})$ and minimum $s \propto \min(T_A^{part}, T_B^{part})$ functions. The generalized Equation 17 maps different model calculations for suitable values of the parameter p. The Glauber wounded nucleon model (WNM), with $s \propto T_A^{part} + T_B^{part}$, is equivalent to the generalized mean ansatz with $p = 1$. The IP-Glasma approach—which combines CGC effects of the incoming gluon distributions, where the gluon thickness function $T_g(b)$ is a Gaussian function of the impact parameter (from the center of the probed nucleon) with a width constrained by HERA DIS data (169), with an event-by-event classical Yang–Mills evolution of the produced glasma gluon fields—deposits density following $T_A^{part} \cdot T_B^{part}$. The default entropy deposition parameter $p = 0$ of T$_R$ENTo, derived from a global fit to multiple experimental data, produces similar initial eccentricities to IP-Glasma (168). In the KLN model, the gluon multiplicity N_g can be determined perturbatively in the k_T-factorization CGC approach from the parton saturation momenta of each nucleus $Q_{sat}^2 \propto T_A$, leading to $s \propto T_{min}\left[2 + \log(T_{max}/T_{min})\right]$. This would correspond to a parameter $p \approx -0.67$ in the generalized ansatz given by Equation 17. The EKRT approach combines collinear factorized pQCD minijet production with a simple model of gluon saturation and predicts an energy density given by $\varepsilon_0 \propto Q_{sat}^3$ with saturation momentum $Q_{sat} = f(T_A, T_B)$, corresponding to an exponent $p \approx 0$.

Smaller, more negative, values of p pull the generalized mean toward a minimum function and hence correspond to models with more extreme gluon saturation effects, leading to the following schematic hierarchy of more saturated initial conditions: WNM < IP-Glasma, T$_R$ENTo, EKRT < MC-KLN. Of course, such a hierarchy accounts only for average density effects, and the different approaches also feature key physics differences that lead to more (or less) QGP shape fluctuations and, thereby, larger (or smaller) eccentricities ε_n that significantly affect the extractions of, for instance, the medium viscosity/overentropy (η/s) ratio from comparisons of measured azimuthal flow coefficients v_n with the hydrodynamics predictions. In particular, the IP-Glasma model also generates the full energy–momentum tensor of the medium with momentum anisotropies with a length scale [of the order of $Q_s^{-1}(x) = 0.1$–0.2 fm] smaller than those present in other calculations (0.4–1 fm), resulting in a finer structure of the initial entropy density compared with the MC-KLN and MCG models (163).

At the LHC, elliptic v_2 and triangular v_3 flows have been studied by, for instance, the ALICE Collaboration in Xe+Xe and Pb+Pb collisions at $\sqrt{s_{NN}} = 5.44$ and 5.02 TeV, respectively. **Figure 6** shows the ratios of $v_{2,3}/\varepsilon_{2,3}$ as a function of particle transverse density [given by $(1/A_\perp)\mathrm{d}N_{ch}/\mathrm{d}\eta$], where ε_n and $A_\perp$ are derived from the initial conditions of various models described above. The hydrodynamics expectation is that v_n/ε_n increases monotonically with the transverse density across different collision energies and systems, and a violation of such a scaling may indicate an incorrect modeling of the initial transverse area $A_\perp$ and/or the azimuthal anisotropies ε_n. The results of **Figure 6** indicate that the standard MCG model using nucleons (panel *a*) and the MC-KLN model (panel *b*) fail to reproduce the expected scalings for v_2 (red symbols), whereas the T$_R$ENTo model with $p = 0$ (equivalent to IP-Glasma) (panel *c*) and the MCG model with constituent partons (panel *d*) feature better scaling behaviors across flow

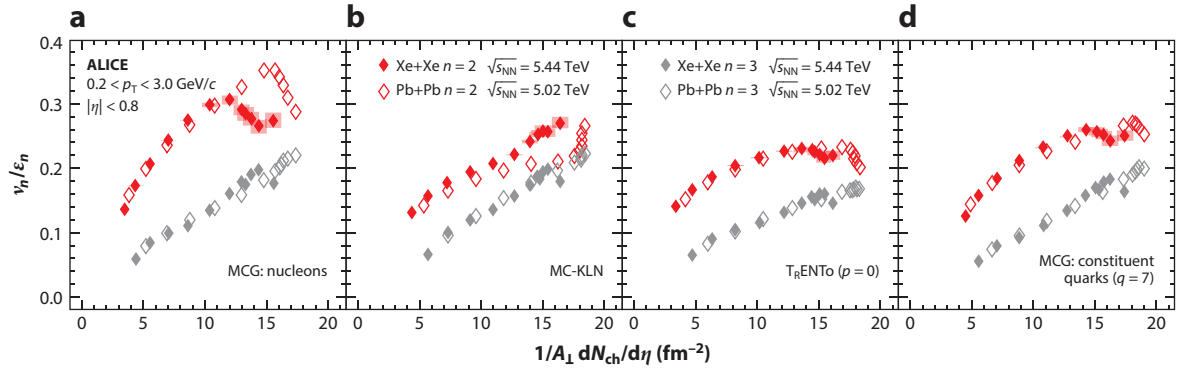

Figure 6

Comparisons of the ratio v_n/ε_n (for $n = 2$ and 3) as a function of particle transverse density, $(1/A_\perp)dN_{ch}/d\eta$, in Xe+Xe and Pb+Pb collisions at the CERN Large Hadron Collider, where v_n and $dN_{ch}/d\eta$ have been measured by the ALICE Collaboration, and the ε_n and $A_\perp$ parameters are derived using the initial conditions of various models. Abbreviations: MC, Monte Carlo; MCG, MC Glauber. Figure adapted from Reference 170 (CC BY 4.0, copyright CERN).

coefficients and systems (although a drop at the largest densities is observed). These results illustrate the types of constraints imposed by the data on initial-conditions medium models, which in this case suggest the need for a higher number of subnucleonic sources in order to achieve a steady increase of $v_{2,3}/\varepsilon_{2,3}$ for more central collisions.

Implications for the extraction of QGP transport properties, such as its viscosity constrained from the experimental ratio of triangular over elliptic flows (v_3/v_2), have also been studied—for instance, in References 120 and 121 for U+U collisions at RHIC energies. The work described in Reference 120 indicates that a model overestimation of the $\varepsilon_3/\varepsilon_2$ ratio will imply a larger amount of the viscous damping needed in the subsequent theoretical hydrodynamics evolution to match the experimental U+U data. A critical comparison of initial conditions derived from IP-Glasma and MCG models for light systems produced in p+Au and d+Au collisions at RHIC can be found in Reference 171.

5. EXPERIMENTAL DEVELOPMENTS

On the experimental front, the LHC data have provided a wealth of new results that have helped to improve the extraction of relevant quantities with the Glauber approach. We review here two experimental aspects that are important in determining the reaction centrality in pA and AA collisions. The centrality determination, a proxy for the (arguably) most important variable of Glauber models—the collision impact parameter—is found to be subject to stronger biases at LHC energies than at lower CM energies.

5.1. Collision Centrality Estimates

As mentioned above, neither the impact parameter nor any derived Glauber quantity can be directly measured experimentally. Instead, average quantities are obtained within Glauber approaches for classes of events whose inclusive particle multiplicities and/or energy distributions can be reproduced by the corresponding calculation over a given b range. Since on average the impact parameter is monotonically related to the overall particle multiplicity, one typically measures

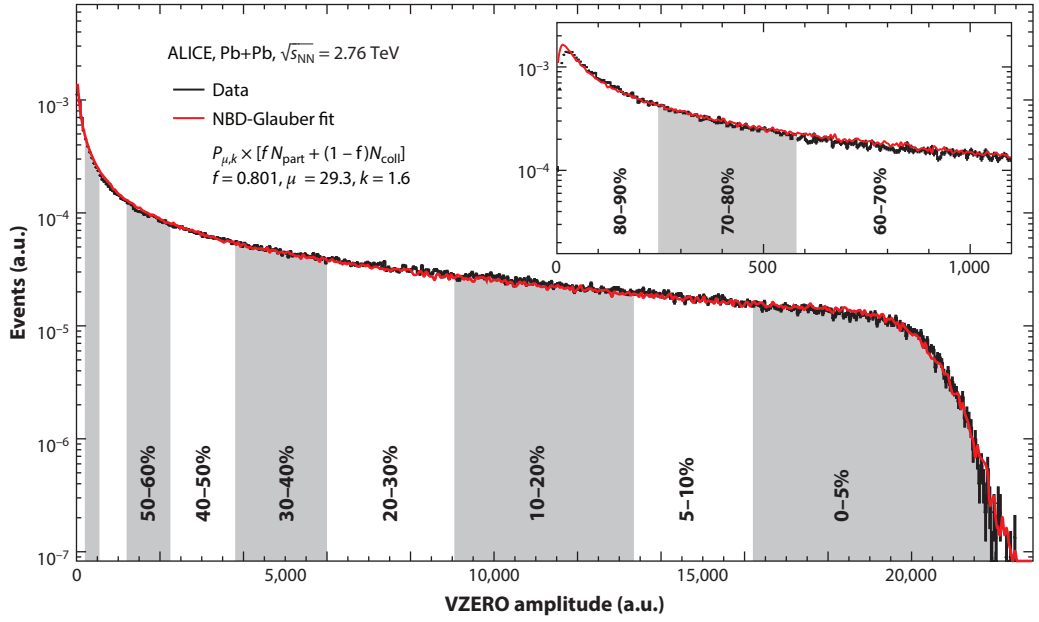

Figure 7

Distribution of the sum of amplitudes (V0M) in the ALICE VZERO detectors measured in Pb+Pb collisions at $\sqrt{s_{NN}} = 2.76$ TeV fitted with the NBD-Glauber model. Centrality classes are indicated by gray boxes. The inset focuses on the most peripheral region. Abbreviation: NBD, negative binomial distribution. Figure adapted from Reference 172 (CC BY 3.0, copyright CERN).

multiplicity (or energy) distributions over a suitably large phase space. The mapping to calculated quantities then proceeds in intervals of centrality or centrality classes, which are obtained by binning the distribution in fractions of its total integral. Centrality is then typically defined as the percentile

$$c_i = \frac{c_{AP}}{M_{tot}} \int_{M_i}^{\infty} \frac{dN}{dM}\, dM \qquad 18.$$

of the per-event multiplicity distribution dN/dM above M_i relative to

$$M_{tot} = \int_{M_{AP}}^{\infty} \frac{dN}{dM}\, dM, \qquad 19.$$

where M_{AP} ($<M_i$) is the multiplicity value for which the fraction of total cross section was determined at the c_{AP} point. The anchor point (AP) sets the absolute scale of the centrality. Clearly, one would like to achieve M_{AP} close to zero, which would result in c_{AP} close to 100%. However, because of trigger inefficiency and the increasing background contamination from ultraperipheral photonuclear collisions, experiments typically can set the AP only between 80% and 90% of the total hadronic cross section. As an example, **Figure 7** shows the sum of the amplitudes in the ALICE VZERO scintillators (at $2.8 < \eta < 5.1$ and $-1.7 < \eta < -3.7$), which is called the V0M centrality estimator and represents the uncorrected charged particle multiplicity distribution. The vertical lines in **Figure 7** indicate the typical centrality binning obtained from slicing

the distribution in fractions of the total integral starting from 90%,[4] where smaller fractions refer to more central collisions.

To determine the AP, one of two approaches is typically used. The first one involves simulation of hadronic and electromagnetic processes, including a detailed description of the detector response, and hence gives direct access to the fraction of hadronic events below M_{AP}. The second one involves MCG modeling, together with a simple description for particle production at the detector level, to simulate the uncorrected multiplicity distribution. The calculated distribution describes the data down to the most peripheral events up to some point where background contamination and trigger inefficiency start to matter. The point at which data and simulation start to separate can be used to set the AP.

To model multiplicity in heavy-ion collisions, one exploits the fact that most initial-state NN collisions can essentially be treated like MB pp collisions, with a small perturbation from rarer hard interactions. The charged particle multiplicity in MB pp collisions at high energy can be described by a negative binomial distribution (NBD) (87) given by

$$P_{\mu,k}(N_{\mathrm{ch}}) = \frac{\Gamma(N_{\mathrm{ch}}+k)}{\Gamma(N_{\mathrm{ch}}+1)\Gamma(k)} \cdot \frac{(\mu/k)^{N_{\mathrm{ch}}}}{(\mu/k+1)^{N_{\mathrm{ch}}+k}}, \qquad 20.$$

where μ is the mean and k is related to the width of the multiplicity distribution. Hence, the multiplicity for heavy-ion events can be approximated as a superposition of many NBDs, quickly approaching the Gaussian limit. A typical approach is to assume that the number of particle-emitting sources can be described by the two-component approach $f \cdot N_{\mathrm{part}} + (1-f) \cdot N_{\mathrm{coll}}$ as in Equation 4. A minimization procedure is then applied to the distribution of hadronic activity to determine the μ, k, and f parameters, with the values listed in **Figure 7** obtained for a χ^2/N_{df} close to unity. The AP can be determined with ∼1% (absolute) uncertainty. The centrality resolution is at the level of a few percent in peripheral collisions and better than 1% in most central collisions.

Because of the finite kinematic acceptance, trigger inefficiency, and detector resolution, as well as the possible biases of the event selection, the details of the centrality determination differ between experiments and even among collision systems within a given experiment. A short introduction with references to the approaches at RHIC is given in Reference 41; for more details on similar approaches at the LHC, we refer the reader to References 172 and 173 for ALICE, Reference 174 for CMS, and Reference 175 for ATLAS. Alternative centrality estimators based on the transverse energy measured at forward rapidities (approximately $3 < |\eta| < 5$ for CMS and ATLAS), as well as far-forward neutral energy in zero degree calorimeters (ZDCs) along the beam line (172, 176), have also been employed. The same methods can be applied to determine the centrality in pA or d+Au collisions (177–179). However, unlike for collisions of larger nuclei, the centrality determination is often subject to larger biases due to fluctuations in the categorization of events (see Section 5.2).

5.2. Collision Centrality Biases

As discussed in Section 4.1, medium effects on the yields of perturbative probes of the QGP are in general quantified by the nuclear modification factor (Equation 16), defined as the ratio of the per-event yield measured in AA collisions over the same yield expected from an incoherent superposition of N_{coll} binary pp collisions. However, event centrality classification involves selection of event samples for which the properties of the underlying binary NN collisions may deviate from

[4]The range 90–100% is prone to potentially large contamination from photonuclear contributions and is therefore often avoided.

those of unbiased pp collisions (84). In this case, R_{AA} (and R_{pA}) can deviate from unity even in the absence of nuclear effects. There are two main sources of selection bias. First, the number of hard processes is suppressed for increasingly peripheral AA collisions because of a simple geometric bias: The probability for collisions increases proportionally to b while the nuclear density decreases, leading to an increased probability for more-peripheral-than-average NN collisions. Second, the centrality selection, which relies mostly on measurements dominated by soft final-state particles (the relative weight of soft-to-hard contributions to the total energy distribution is given by the $f \approx 0.8$ parameter in **Figure 7**), biases the average multiplicity of individual NN collisions and therefore can affect the normalization of yields of collisions dominated by hard processes. As shown in **Figure 3*a***, hard scatterings are more probable in central NN collisions with large partonic overlap, which leads to many simultaneous MPIs with lots of UE activity, and since hard processes are dominated by the production of jets that fragment (or heavy resonances that decay) into a large number of final hadrons, a peripheral AA event with a hard scattering often has a hadronic activity much larger than what is typical of its centrality class. Since the AA (and pA) centrality determination is based on ordering the measured multiplicity or summed energy in the event, peripheral nuclear events with a hard scattering can thereby be wrongly assigned to a more central class.

The geometric effect can be included in optical Glauber calculations by extending Equation 3 with a convolution of the nuclear thickness functions (depending on the overall b) with the NN overlap function (T_{NN}, depending on the b_{NN} impact parameter) as

$$T'_{AB}(\mathbf{b}) = \int d^2s\, d^2b_{NN}\, T_A(\mathbf{s})\, T_B(\mathbf{s} - \mathbf{b} + \mathbf{b}_{NN})\, T_{NN}(\mathbf{b}_{NN}), \quad 21.$$

which effectively leads to a reduction of N_{coll} in peripheral collisions compared with $T_{NN} = \delta(b_{NN})$ because of their increased probability for less-central-than-average NN collisions. Standard MCG calculations, which by construction include the geometric bias, do not use information about individual NN collisions. Even though the NN collisions are still modeled as occurring incoherently, the number of hard processes for a given centrality selection is taken not proportionally to N_{coll} but instead to

$$N_{hard} = N_{coll} \cdot N_{NN}^{hard} / \left\langle N_{NN}^{hard} \right\rangle, \quad 22.$$

where N_{NN}^{hard} is the average number of hard scatterings in an NN collision for a given centrality selection and $\langle N_{NN}^{hard} \rangle$ is its unbiased average value. The mean number of hard scatterings per collision depends on b_{NN} and can be written as $N_{hard}(b_{NN}) = \sigma_{hard}\, T_{NN}(b_{NN})$, where σ_{hard} is the pQCD cross section for $2 \to 2$ parton scatterings. Since the yields of hard and soft processes are correlated via their common b_{NN}, the NN collisions can be biased toward lower- or higher-than-average impact parameters when ordering the measured multiplicity or transverse energy necessary for the centrality determination. This fact leads to a selection bias on N_{NN}^{hard} in addition to the inherent geometric bias. Because of the strong dependence of σ_{hard} on $\sqrt{s}$, the selection bias is more relevant at LHC than at RHIC (and negligible at SPS) collision energies.

The relevance of the selection bias induced by the correlation between soft and hard particles is demonstrated in **Figure 8**, which shows the nuclear modification factors for charged particle production, integrated above a large enough p_T value (8 and 10 GeV), in p+Pb and Pb+Pb collisions at $\sqrt{s_{NN}} = 5.02$ TeV compared with calculations using HG-Pythia (84). The calculation, which uses the Hijing model to determine the distribution of $N_{hard}(b_{NN})$ in a nuclear collision and Pythia 6.28 (Perugia 2011 tune) to generate the corresponding NN events, purposely does not include nuclear modification effects, unlike most of the models discussed in Section 4.2. As for the data, where the V0M estimator was used, the calculation determines the centrality using charged

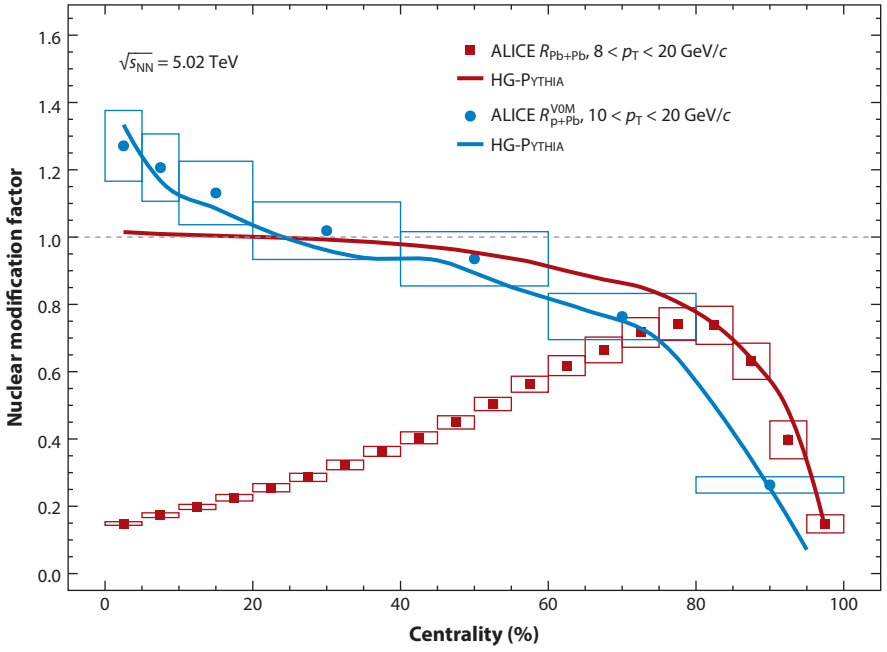

Figure 8

Nuclear modification factors for high-p_T charged particles (above 8 or 10 GeV) as a function of centrality in p+Pb (*blue circles*) and Pb+Pb (*red squares*) collisions at $\sqrt{s_{NN}} = 5.02$ TeV (178, 180) compared with calculations using HG-PYTHIA (84) (*blue* and *red curves*).

particles in the acceptance of the ALICE VZERO detectors. The calculation accurately describes the p+Pb and very peripheral Pb+Pb data and indicates that the strong apparent suppression from unity in this region results, in both cases, from the event selection. For more central Pb+Pb collisions, where parton energy loss leads to the known large suppression of particle production in Pb+Pb compared with pp collisions, the R_{AA} is not affected by such biases.

The hard–soft event selection bias is particularly important when fluctuations of the centrality estimator caused by b_{NN} are similar in size to the dynamic range of N_{coll} (as is the case in pA collisions) and is strongly enhanced by trivial autocorrelations if the phase spaces for the measurement and event categorization are nearby or overlap (177–179). The presence of a bias can be deduced by computing the ratio between the average multiplicity of the centrality estimator and the average multiplicity per average ancestor of the Glauber fit as demonstrated in figure 8 of Reference 178. In contrast, centrality measurements based on zero-degree energy should not introduce any selection bias, but the geometric bias could still play a role. In the so-called hybrid method (178), the p+Pb centrality selection is based on ZDC neutral energy in the Pb-going directions (slow neutrons), and N_{coll} is determined from the measured charged particle multiplicity M according to $N_{coll} = \langle N_{coll}\rangle \cdot M/\langle M\rangle$, where $\langle N_{coll}\rangle$ and $\langle M\rangle$ are, respectively, the centrality-averaged number of collisions and multiplicity. If soft and hard particle yields are affected in the same way, the selection bias will cancel out in the nuclear modification factor.

6. SUMMARY

An outstanding topic in the physics of the strong interaction concerns the thermodynamic and transport properties of hot and dense quark–gluon matter accessible to experimental study via

high-energy collisions of nuclei. To correctly identify and interpret signals of collective partonic behavior in AA collisions, one needs a realistic extrapolation of the baseline hadron production properties of pp and pA collisions in which, in principle, no QGP is expected to be formed. The Glauber model allows for arguably the simplest and most economical, yet successful, understanding of collisions of extended hadronic objects based on an impact parameter b superposition of independent elementary scatterings, each of which produces particles and thereby defines the local and global density of the precursor QGP. Key derived quantities in Glauber models include the nuclear overlap function $T_{\mathrm{AA}}(b)$, number of participant nucleons $N_{\mathrm{part}}(b)$, number of binary collisions $N_{\mathrm{coll}}(b)$, transverse area $A_{\perp}(b)$, eccentricities $\varepsilon_n(b)$, and average path length $L(b)$ of the strongly interacting medium produced at different collision centralities, which are fundamental to the extraction of the QGP properties from the data. In this article, we have reviewed the main developments and the state of the art of the Glauber approach to describe multiple scatterings in proton and nuclear collisions after 10 years of operation with pp, p+Pb, and Pb+Pb collisions at the LHC as well as with deformed light and heavy ions at RHIC.

The new LHC measurements (performed at CM energies 50 times larger than those at previous nuclear collisions) and the latest precision RHIC data for a variety of colliding systems have required us to revisit and improve various ingredients of the MCG simulations. Our review has first provided a new fit of the world measurements of the inclusive inelastic nucleon–nucleon cross sections (σ_{NN}), a key ingredient of MCG models. The inelastic hadronic pA and AA cross sections measured at the LHC are well reproduced by the corresponding MCG results derived using σ_{NN}, a fact that confirms the overall validity of the Glauber model at the highest CM energies studied to date. Second, improved descriptions of the proton and nuclear density profiles, including subnucleonic degrees of freedom and neutron skin effects and any associated sources of fluctuations and correlations, have been examined. Third, we have reviewed the main applications of the Glauber model for collider studies. The binary scaling prescription to quantitatively compare hard scattering cross sections in pp, pA, and AA collisions has been validated by measurements of electroweak probes at the LHC whose yields are unaffected by final-state interactions in the QGP. The use of the Glauber formalism in MC event generators for heavy-ion physics, as well as to provide initial entropy–density profiles as input for relativistic hydrodynamics calculations, has also been discussed. The importance of a realistic description of the medium eccentricities to extract key transport properties (e.g., the QGP shear viscosity), from comparisons of elliptic and triangular flow measurements at the LHC and RHIC with viscous hydrodynamics predictions, has been highlighted. Last, the experimental procedures used and the inherent biases introduced by them in the determination of the collision centrality from the data, which rely on the application of the MCG model, have been briefly discussed.

As an illustrative summary of our review, **Figure 9** shows the impact of different Glauber model ingredients and experimental biases, presented as a ratio as a function of centrality of the different elements over the default standard MCG calculation, for Pb+Pb collisions at $\sqrt{s_{\mathrm{NN}}} = 5.5$ TeV (**Figure 9*a***) and p+Pb collisions at $\sqrt{s_{\mathrm{NN}}} = 8.8$ TeV (**Figure 9*b***). The dashed red curves in **Figure 9** indicate the magnitude of the experimental shift introduced in measured nuclear modification factors when not properly accounting for event selection (multiplicity- and process-dependent) biases introduced by the centrality determination. These biases are significant in the most peripheral centrality classes and need to be carefully modeled and/or corrected for, especially when aiming at precision measurements for large impact parameters. The other curves in **Figure 9** indicate the ratio of the values of N_{coll} obtained with modified ingredients with respect to standard MCG simulations. Inclusion of Glauber–Gribov fluctuations (via Equation 10 with $\Omega = 1.0$), modified NN collision profiles (via Equation 9 with $\omega = 0.4$), or neutron skin effects leads to

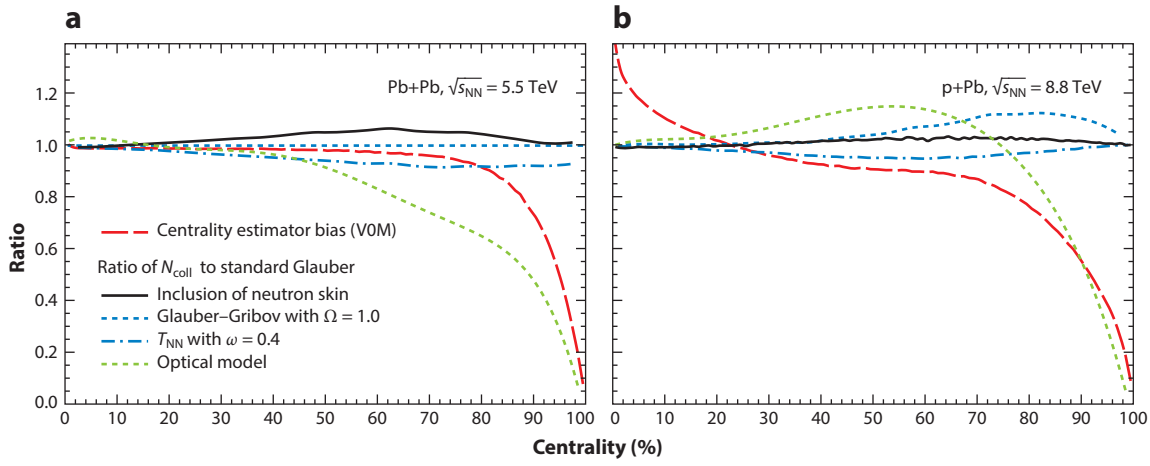

Figure 9

Ratio of N_{coll} as a function of centrality in (*a*) Pb+Pb and (*b*) p+Pb collisions at the CERN Large Hadron Collider obtained with the various model developments discussed in this review, and for the optical limit (see Equation 3) normalized to the result obtained with the conventional Monte Carlo Glauber model. In addition, the bias induced by the centrality determination is shown for a typical experimental estimator (ALICE V0M, *dashed red curves*).

few-percent modifications of the N_{coll} values in different centrality ranges, in principle within the assigned Glauber model systematic uncertainties (18). An analytical calculation of N_{coll} in the optical Glauber limit leads, however, to significant underestimations of the number of collisions for peripheral Pb+Pb and p+Pb collisions.

The results shown in **Figure 9** emphasize the need for large quantitative corrections in the Glauber model for the most peripheral AA and pA collisions. The availability of very large data samples of electroweak bosons at the LHC with cross section measurements with few-percent experimental uncertainties similar to or smaller than those of the Glauber model raises the possibility of using them to define an alternative experimental proxy for the nuclear overlap function. The ratio $N_V/(\sigma^V_{NN} N_{evt})$, where σ^V_{NN} is the vector boson ($V = \sum W^{\pm}, Z$) production cross section in NN collisions (which can be estimated from pp measurements) and N_V/N_{evt} indicates the per-event AA yields, has been suggested (181) as a data-driven $T_{AA}(b)$ proxy that would eliminate the need for Glauber modeling and reduce corrections for centrality and event selection effects while canceling out uncertainties in the determination of quantities such as R_{AA}. Such a proposal would require a higher level of theoretical accuracy (NNLO) in the nuclear PDFs and in their centrality dependence to fully exploit the high-precision σ^V_{pp} measurements.

All in all, the results summarized in this review show that despite its simplicity (or, arguably, thanks to it), the Glauber model has stood for over 50 years as an indispensable and useful baseline approach to quantitatively compare collisions of systems of varying size, from protons to uranium nuclei. Its continued ability to extract from the data key thermodynamic and transport properties of strongly interacting matter at the highest densities and temperatures accessible in the laboratory will likely remain unchallenged for years to come.

DISCLOSURE STATEMENT

The authors are not aware of any affiliations, memberships, funding, or financial holdings that might be perceived as affecting the objectivity of this review.

ACKNOWLEDGMENTS

We are indebted to J. Kamin, A. Morsch, J. Nagle, A. Snigirev, and P. Steinberg for common work and discussions in the past years leading to results presented in this review. Comments on the text by W. Busza, U. Heinz, I. Helenius, V. Kovalenko, H. Paukkunen, and B. Schenke are gratefully acknowledged. We thank F. Jonas for carefully reading the manuscript. C.L. is supported by the US Department of Energy, Office of Science, Office of Nuclear Physics, under contract number DE-AC05-00OR22725.

LITERATURE CITED

1. Busza W, Rajagopal K, van der Schee W. *Annu. Rev. Nucl. Part. Sci.* 68:339 (2018)
2. Borsanyi S, et al. *Phys. Lett. B* 730:99 (2014)
3. Bazavov A, et al. (HotQCD Collab.) *Phys. Rev. D* 90:094503 (2014)
4. d'Enterria D. *J. Phys. G* 34:S53 (2007)
5. Martin P, Glauber R. *Phys. Rev.* 109:1307 (1958)
6. Glauber RJ, Matthiae G. *Nucl. Phys. B* 21:135 (1970)
7. Czyz W, Maximon L. *Ann. Phys.* 52:59 (1969)
8. Bialas A, Bleszynski M, Czyz W. *Nucl. Phys. B* 111:461 (1976)
9. Bialas A, Bleszynski M, Czyz W. *Acta Phys. Polon. B* 8:389 (1977)
10. Wang XN, Gyulassy M. *Phys. Rev. D* 44:3501 (1991)
11. Broniowski W, Rybczynski M, Bozek P. *Comput. Phys. Commun.* 180:69 (2009)
12. Alver B, Baker M, Loizides C, Steinberg P. arXiv:0805.4411 [nucl-ex] (2008)
13. Alvioli M, Drescher HJ, Strikman M. *Phys. Lett. B* 680:225 (2009)
14. Rybczynski M, Stefanek G, Broniowski W, Bozek P. *Comput. Phys. Commun.* 185:1759 (2014)
15. Loizides C, Nagle J, Steinberg P. *SoftwareX* 1–2:13 (2015)
16. Loizides C. *Phys. Rev. C* 94:024914 (2016)
17. Mitchell JT, Perepelitsa DV, Tannenbaum MJ, Stankus PW. *Phys. Rev. C* 93:054910 (2016)
18. Loizides C, Kamin J, d'Enterria D. *Phys. Rev. C* 97:054910 (2018). Erratum. *Phys. Rev. C* 99:019901 (2019); Loizides C, Kamin J, d'Enterria D. TGlauberMC, version 3. *Modeling Software*. **https://tglaubermc.hepforge.org/** (2017)
19. Bożek P, Broniowski W, Rybczynski M, Stefanek G. *Comput. Phys. Commun.* 245:106850 (2019)
20. De Jager CW, De Vries H, De Vries C. *At. Data Nucl. Data Tables* 14:479 (1974)
21. De Vries H, De Jager CW, De Vries C. *At. Data Nucl. Data Tables* 36:495 (1987)
22. Heinz U, Snellings R. *Annu. Rev. Nucl. Part. Sci.* 63:123 (2013)
23. Wang XN, Gyulassy M. *Phys. Rev. Lett.* 86:3496 (2001)
24. Acharya S, et al. (ALICE Collab.) *Phys. Rev. C* 101:044907 (2020)
25. Ollitrault JY. *Phys. Rev. D* 46:229 (1992)
26. Romatschke P. *Int. J. Mod. Phys. E* 19:1 (2010)
27. Teaney DA. Viscous hydrodynamics and the quark gluon plasma. In *Quark-Gluon Plasma*, Vol. 4, ed. RC Hwa, X-N Wang, pp. 207–66. Singapore: World Sci. (2010)
28. Luzum M, Romatschke P. *Phys. Rev. Lett.* 103:262302 (2009)
29. Schenke B, Jeon S, Gale C. *Phys. Rev. Lett.* 106:042301 (2011)
30. Weller RD, Romatschke P. *Phys. Lett. B* 774:351 (2017)
31. Alver B, Roland G. *Phys. Rev. C* 81:054905 (2010). Erratum. *Phys. Rev. C* 82:039903 (2010)
32. Aamodt K, et al. (ALICE Collab.) *Phys. Rev. Lett.* 107:032301 (2011)
33. Adare A, et al. (PHENIX Collab.) *Phys. Rev. Lett.* 107:252301 (2011)
34. Aad G, et al. (ATLAS Collab.) *Phys. Rev. C* 86:014907 (2012)
35. Chatrchyan S, et al. (CMS Collab.) *Phys. Lett. B* 724:213 (2013)
36. Dainese A, Loizides C, Paic G. *Eur. Phys. J. C* 38:461 (2005)
37. Lokhtin I, Snigirev A. *Eur. Phys. J. C* 45:211 (2006)
38. Djordjevic M, Zigic D, Djordjevic M, Auvinen J. *Phys. Rev. C* 99:061902 (2019)

39. d'Enterria D. Jet quenching. In *Landolt-Börnstein—Group I Elementary Particles, Nuclei and Atoms*, Vol. 23: *Relativistic Heavy Ion Physics*, ed. R Stock. Berlin: Springer. **https://doi.org/10.1007/978-3-642-01539-7_16** (2010)
40. Baltz A, et al. *Phys. Rep.* 458:1 (2008)
41. Miller ML, Reygers K, Sanders SJ, Steinberg P. *Annu. Rev. Nucl. Part. Sci.* 57:205 (2007)
42. Alver B, et al. (PHOBOS Collab.) *Phys. Rev. C* 83:024913 (2011)
43. Abada A, et al. (FCC Collab.) *Eur. Phys. J. Spec. Top.* 228:755 (2019)
44. Tanabashi M, et al. (Part. Data Group) *Phys. Rev. D* 98:030001 (2018)
45. Alner GJ, et al. (UA5 Collab.) *Z. Phys. C* 32:153 (1986)
46. Amos NA, et al. (E710 Collab.) *Phys. Lett. B* 243:158 (1990)
47. Amos NA, et al. (E710 Collab.) *Phys. Rev. Lett.* 68:2433 (1992)
48. Abe F, et al. (CDF Collab.) *Phys. Rev. D* 50:5550 (1994)
49. Abe F, et al. (CDF Collab.) *Phys. Rev. D* 50:5518 (1994)
50. Adam J, et al. (STAR Collab.) *Phys. Lett. B* 808:135663 (2020)
51. Abelev B, et al. (ALICE Collab.) *Eur. Phys. J. C* 73:2456 (2013)
52. Aad G, et al. (ATLAS Collab.) *Nat. Commun.* 2:463 (2011)
53. Aad G, et al. (ATLAS Collab.) *Nucl. Phys. B* 889:486 (2014)
54. Aaboud M, et al. (ATLAS Collab.) *Phys. Lett. B* 761:158 (2016)
55. Aaboud M, et al. (ATLAS Collab.) *Phys. Rev. Lett.* 117:182002 (2016)
56. Chatrchyan S, et al. (CMS Collab.) *Phys. Lett. B* 722:5 (2013)
57. Sirunyan AM, et al. (CMS Collab.) *J. High Energy Phys.* 1807:161 (2018)
58. Aaij R, et al. (LHCb Collab.) *J. High Energy Phys.* 1502:129 (2015)
59. Aaij R, et al. (LHCb Collab.) *J. High Energy Phys.* 1806:100 (2018)
60. Antchev G, et al. (TOTEM Collab.) *Europhys. Lett.* 96:21002 (2011)
61. Antchev G, et al. (TOTEM Collab.) *Europhys. Lett.* 101:21004 (2013)
62. Antchev G, et al. (TOTEM Collab.) *Phys. Rev. Lett.* 111:012001 (2013)
63. Antchev G, et al. (TOTEM Collab.) *Eur. Phys. J. C* 79:103 (2019)
64. Cafagna F. (TOTEM Collab.) *Proc. Sci.* ICRC2019:207 (2020)
65. Abreu P, et al. (Pierre Auger Collab.) *Phys. Rev. Lett.* 109:062002 (2012)
66. Cudell JR, et al. (COMPETE Collab.) *Phys. Rev. Lett.* 89:201801 (2002)
67. d'Enterria D, Pierog T. *J. High Energy Phys.* 1608:170 (2016)
68. Abelev B, et al. (ALICE Collab.) *Phys. Rev. Lett.* 109:252302 (2012)
69. Khachatryan V, et al. (CMS Collab.) *Phys. Lett. B* 759:641 (2016)
70. Abelev BB, et al. (ALICE Collab.) *J. Instrum.* 9:P11003 (2014)
71. Sjöstrand T, et al. *Comput. Phys. Commun.* 191:159 (2015)
72. Bahr M, et al. *Eur. Phys. J. C* 58:639 (2008)
73. Field R. *Acta Phys. Polon. B* 42:2631 (2011)
74. d'Enterria D, Snigirev A. Double, triple, and *n*-parton scatterings in high-energy proton and nuclear collisions. In *Advanced Series on Directions in High Energy Physics*, Vol. 29: *Multiple Parton Interactions at the LHC*, ed. P Bartalini, JR Gaunt, pp. 159–87. Singapore: World Sci. (2018)
75. Khachatryan V, et al. (CMS Collab.) *J. High Energy Phys.* 1009:91 (2010)
76. Aad G, et al. (ATLAS Collab.) *Phys. Rev. Lett.* 116:172301 (2016)
77. Khachatryan V, et al. (CMS Collab.) *Phys. Lett. B* 765:193 (2017)
78. d'Enterria D, et al. *Eur. Phys. J. C* 66:173 (2010)
79. Hofstadter R. *Rev. Mod. Phys.* 28:214 (1956)
80. Corke R, Sjöstrand T. *J. High Energy Phys.* 1105:9 (2011)
81. Skands P, Carrazza S, Rojo J. *Eur. Phys. J. C* 74:3024 (2014)
82. Acharya S, et al. (ALICE Collab.) *Eur. Phys. J. C* 79:857 (2019)
83. Sjöstrand T. The development of MPI modeling in Pythia. In *Advanced Series on Directions in High Energy Physics*, Vol. 29: *Multiple Parton Interactions at the LHC*, ed. P Bartalini, JR Gaunt, pp. 191–225. Singapore: World Sci. (2018)

84. Loizides C, Morsch A. *Phys. Lett. B* 773:408 (2017)
85. Alvioli M, Holopainen H, Eskola KJ, Strikman M. *Phys. Rev. C* 85:034902 (2012)
86. Rybczyński M, Wlodarczyk Z. *J. Phys. G* 41:015106 (2013)
87. Grosse-Oetringhaus JF, Reygers K. *J. Phys. G* 37:083001 (2010)
88. Welsh K, Singer J, Heinz UW. *Phys. Rev. C* 94:024919 (2016)
89. Moreland JS, Bernhard JE, Bass SA. *Phys. Rev. C* 101:024911 (2020)
90. Teaney D, Yan L. *Phys. Rev. C* 83:064904 (2011)
91. Alver B, et al. (PHOBOS Collab.) *Phys. Rev. Lett.* 98:242302 (2007)
92. Blaizot JP, Broniowski W, Ollitrault JY. *Phys. Rev. C* 90:034906 (2014)
93. Heiselberg H, et al. *Phys. Rev. Lett.* 67:2946 (1991)
94. Alvioli M, Strikman M. *Phys. Lett. B* 722:347 (2013)
95. Alvioli M, Frankfurt L, Perepelitsa D, Strikman M. *Phys. Rev. D* 98:071502 (2018)
96. Gribov V. *Sov. Phys. JETP* 29:483 (1969)
97. Bierlich C, Gustafson G, Lönnblad L. *J. High Energy Phys.* 1610:139 (2016)
98. Adare A, et al. (PHENIX Collab.) *Phys. Rev. Lett.* 116:122301 (2016)
99. Aad G, et al. (ATLAS Collab.) *Eur. Phys. J. C* 76:199 (2016)
100. McGlinchey D, Nagle J, Perepelitsa D. *Phys. Rev. C* 94:024915 (2016)
101. Ciofi degli Atti C, et al. *Phys. Rev. C* 84:025205 (2011)
102. Flensburg C, Gustafson G, Lönnblad L. *J. High Energy Phys.* 1108:103 (2011)
103. Salam G. *J. High Energy Phys.* 9807:019 (1998)
104. Barrett RC, Jackson DF. *Nuclear Sizes and Structure*. Oxford, UK: Oxford Univ. Press (1977)
105. Klos B, et al. *Phys. Rev. C* 76:014311 (2007)
106. Tarbert CM, et al. *Phys. Rev. Lett.* 112:242502 (2014)
107. Fricke G, et al. *At. Data Nucl. Data Tables* 60:177 (1995)
108. Horowitz CJ, Pollock SJ, Souder PA, Michaels R. *Phys. Rev. C* 63:025501 (2001)
109. Paukkunen H. *Phys. Lett. B* 745:73 (2015)
110. De S. *J. Phys. G* 44:045104 (2017)
111. Helenius I, Paukkunen H, Eskola KJ. *Eur. Phys. J. C* 77:148 (2017)
112. Alvioli M, Strikman M. *Phys. Rev. C* 100:024912 (2019)
113. Durham JM. (PHENIX Collab.) *Proc. Sci.* HardProbes2018:165 (2018)
114. Adamczyk L, et al. (STAR Collab.) *Phys. Rev. Lett.* 115:222301 (2015)
115. Hulthén L, Sugawara M. The two-nucleon problem. In *Encyclopedia of Physics*, Vol. 39: *Structure of Atomic Nuclei*, ed. S Flügge, pp. 1–143. Berlin/Heidelberg: Springer (1957)
116. Adler SS, et al. (PHENIX Collab.) *Phys. Rev. Lett.* 91:072303 (2003)
117. Adler SS, et al. (PHENIX Collab.) *Phys. Rev. C* 74:024904 (2006)
118. Nagle JL, et al. *Phys. Rev. Lett.* 113:112301 (2014)
119. Lim S, et al. *Phys. Rev. C* 99:044904 (2019)
120. Shou QY, et al. *Phys. Lett. B* 749:215 (2015)
121. Noronha-Hostler J, et al. arXiv:1905.13323 [hep-ph] (2019)
122. Giacalone G. *Phys. Rev. Lett.* 124:202301 (2020)
123. Huang S, Chen Z, Jia J, Li W. *Phys. Rev. C* 101:021901 (2020)
124. Sievert MD, Noronha-Hostler J. *Phys. Rev. C* 100:024904 (2019)
125. Vogt R. *Acta Phys. Hung. A* 9:339 (1999)
126. d'Enterria D. arXiv:nucl-ex/0302016 (2003)
127. Adler S, et al. (PHENIX Collab.) *Phys. Rev. Lett.* 94:232301 (2005)
128. Chatrchyan S, et al. (CMS Collab.) *Phys. Lett. B* 710:256 (2012)
129. Aad G, et al. (ATLAS Collab.) *Phys. Rev. C* 93:034914 (2016)
130. Sirunyan AM, et al. (CMS Collab.) *J. High Energy Phys.* 2007:116 (2020)
131. Aad G, et al. (ATLAS Collab.) *Phys. Rev. Lett.* 110:022301 (2013)
132. Aad G, et al. (ATLAS Collab.) *Eur. Phys. J. C* 75:23 (2015)

133. Aad G, et al. (ATLAS Collab.) *Phys. Rev. C* 92:044915 (2015)
134. Khachatryan V, et al. (CMS Collab.) *Phys. Lett. B* 759:36 (2016)
135. Acharya S, et al. (ALICE Collab.) *Phys. Lett. B* 780:372 (2018)
136. Aad G, et al. (ALICE Collab.) *Phys. Lett. B* 802:135262 (2020)
137. Aad G, et al. (ALICE Collab.) *Eur. Phys. J. C* 79:935 (2019)
138. Sirunyan AM, et al. (CMS Collab.) *Phys. Lett. B* 800:135048 (2020)
139. Eskola KJ, Paakkinen P, Paukkunen H, Salgado CA. *Eur. Phys. J. C* 77:163 (2017)
140. Kusina A, et al. *Eur. Phys. J. C* 77:488 (2017)
141. Abdul Khalek R, Ethier JJ, Rojo J, van Weelden G. *J. High Energy Phys.* 2009:183 (2020)
142. Khanpour H, Atashbar Tehrani S. *Phys. Rev. D* 93:014026 (2016)
143. Eskola KJ, Helenius I, Kuha M, Paukkunen H. *Phys. Rev. Lett.* 125:212301 (2020)
144. Deng WT, Wang XN, Xu R. *Phys. Rev. C* 83:014915 (2011)
145. Pierog T, et al. *Phys. Rev. C* 92:034906 (2015)
146. Lin ZW, et al. *Phys. Rev. C* 72:064901 (2005)
147. Ostapchenko S. *Phys. Rev. D* 83:014018 (2011)
148. Roesler S, Engel R, Ranft J. The Monte Carlo event generator DPMJET-III. In *Advanced Monte Carlo for Radiation Physics, Particle Transport Simulation and Applications: Proceedings of the Monte Carlo 2000 Conference, Lisbon, 23–26 October 2000*, ed. A Kling, et al., pp. 1033–38. Berlin: Springer (2001)
149. Sjöstrand T, Mrenna S, Skands PZ. *Comput. Phys. Commun.* 178:852 (2008)
150. Bierlich C, Gustafson G, Lönnblad L, Shah H. *J. High Energy Phys.* 1810:134 (2018)
151. d'Enterria D, et al. *Astropart. Phys.* 35:98 (2011)
152. Andersson B. *The Lund Model*, Vol. 7. Cambridge, UK: Cambridge Univ. Press (2005)
153. Andersson B, Gustafson G, Nilsson-Almqvist B. *Nucl. Phys. B* 281:289 (1987)
154. Klein SR, et al. *Comput. Phys. Commun.* 212:258 (2017)
155. Harland-Lang L, Khoze V, Ryskin M. *Eur. Phys. J. C* 79:39 (2019)
156. Heinz U. Early collective expansion: relativistic hydrodynamics and the transport properties of QCD matter. In *Landolt-Börnstein—Group I Elementary Particles, Nuclei and Atoms*, Vol. 23: *Relativistic Heavy Ion Physics*, ed. R Stock. Berlin: Springer. **https://doi.org/10.1007/978-3-642-01539-7_9** (2010)
157. Hirano T, Huovinen P, Murase K, Nara Y. *Prog. Part. Nucl. Phys.* 70:108 (2013)
158. Gale C, Jeon S, Schenke B. *Int. J. Mod. Phys. A* 28:1340011 (2013)
159. Petersen H, et al. *Phys. Rev. C* 78:044901 (2008)
160. Strickland M. *Pramana* 84:671 (2015)
161. Kharzeev D, Levin E, Nardi M. *Phys. Rev. C* 71:054903 (2005)
162. Drescher HJ, Nara Y. *Phys. Rev. C* 75:034905 (2007)
163. Schenke B, Tribedy P, Venugopalan R. *Phys. Rev. C* 86:034908 (2012)
164. Schenke B, Tribedy P, Venugopalan R. *Phys. Rev. Lett.* 108:252301 (2012)
165. Gelis F, Iancu E, Jalilian-Marian J, Venugopalan R. *Annu. Rev. Nucl. Part. Sci.* 60:463 (2010)
166. Eskola K, Kajantie K, Ruuskanen P, Tuominen K. *Nucl. Phys. B* 570:379 (2000)
167. Niemi H, Eskola K, Paatelainen R. *Phys. Rev. C* 93:024907 (2016)
168. Moreland JS, Bernhard JE, Bass SA. *Phys. Rev. C* 92:011901 (2015)
169. Kowalski H, Teaney D. *Phys. Rev. D* 68:114005 (2003)
170. Acharya S, et al. (ALICE Collab.) *Phys. Lett. B* 784:82 (2018)
171. Nagle J, Zajc W. *Phys. Rev. C* 99:054908 (2019)
172. Abelev B, et al. (ALICE Collab.) *Phys. Rev. C* 88:044909 (2013)
173. Acharya S. (ALICE Collab.) *Centrality determination in heavy ion collisions.* Rep. ALICE-PUBLIC-2018-011, CERN, Geneva. **https://cds.cern.ch/record/2636623** (2018)
174. Chatrchyan S, et al. (CMS Collab.) *J. High Energy Phys.* 1108:141 (2011)
175. Aad G, et al. (ATLAS Collab.) *Phys. Lett. B* 710:363 (2012)
176. Wood JS. 2012. *The development of the CMS zero degree calorimeters to derive the centrality of* AA *collisions*. PhD Diss., Univ. Kansas, Lawrence

177. Adare A, et al. (PHENIX Collab.) *Phys. Rev. C* 90:034902 (2014)
178. Adam J, et al. (ALICE Collab.) *Phys. Rev. C* 91:064905 (2015)
179. Perepelitsa DV, Steinberg PA. arXiv:1412.0976 [nucl-ex] (2014)
180. Acharya S, et al. (ALICE Collab.) *Phys. Lett. B* 793:420 (2019)
181. Sirunyan AM, et al. (CMS Collab.) arXiv:2103.14089 [hep-ex] (2021)